Materials & Design 212 (2021) 110246

Contents lists available at ScienceDirect

Materials & Design

journal homepage: www.elsevier.com/locate/matdes

Strengthening control in laser powder bed fusion of austenitic stainless steels via grain boundary engineering

Hossein Eskandari Sabzi [a], Everth Hernandez-Nava [d], Xiao-Hui Li [b], Hanwei Fu [b,*], David San-Martín [c], Pedro E.J. Rivera-Díaz-del-Castillo [a,*]

[a] Department of Engineering, Engineering Building, Lancaster University, LA1 4YW, United Kingdom
[b] School of Materials Science and Engineering, Beihang University, No. 37 Xueyuan Road, Beijing 100191, China
[c] Materalia Research Group, Physical Metallurgy Department, Centro Nacional de Investigaciones Metalúrgicas (CENIM-CSIC), Avda. Gregorio del Amo 8, 28040 Madrid, Spain
[d] Department of Material Science & Engineering, The University of Sheffield, Sir Robert Hadfield Building, Mappin St, Sheffield S13 JD, United Kingdom

HIGHLIGHTS

- Process/microstructure/strength in laser powder bed fusion are related.
- Yield strength scales with subgrain size through a Hall–Petch-type relationship.
- Dynamic recovery is essential to promote low-angle grain boundaries.
- *In situ* dynamic recovery and recrystallization modelled via two approaches.

GRAPHICAL ABSTRACT

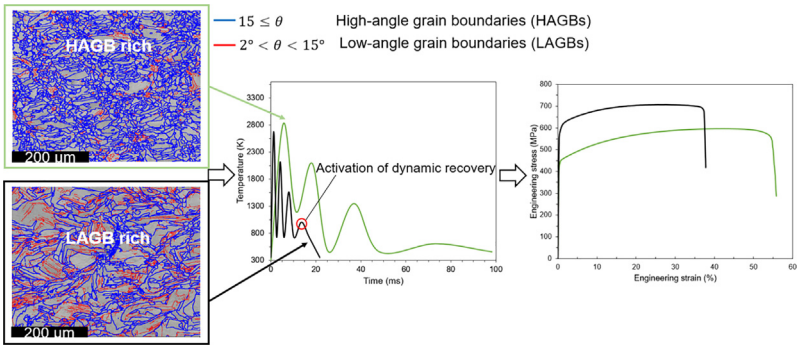

ARTICLE INFO

Article history:
Received 13 September 2021
Revised 8 November 2021
Accepted 9 November 2021
Available online 12 November 2021

Keywords:
Laser powder bed fusion
Mechanical properties
Stainless steel
Grain refinement
Microstructure

ABSTRACT

A new approach to modelling the microstructure evolution and yield strength in laser powder bed fusion components is introduced. Restoration mechanisms such as discontinuous dynamic recrystallization, continuous dynamic recrystallization, and dynamic recovery were found to be activated during laser powder bed fusion of austenitic stainless steels; these are modelled both via classical Zener-Hollomon and thermostatistical approaches. A mechanism is suggested for the formation of dislocation cells from solidification cells and dendrites, and their further transformation to low-angle grain boundaries to form subgrains. This occurs due to dynamic recovery during laser powder bed fusion. The yield strength is successfully modelled via a Hall–Petch-type relationship in terms of the subgrain size, instead of the actual grain size or the dislocation cell size. The validated Hall–Petch-type equation for austenitic stainless steels provides a guideline for the strengthening of laser powder bed fusion alloys with subgrain refinement, via increasing the low-angle grain boundary fraction (grain boundary engineering). To obtain higher strength, dynamic recovery should be promoted as the main mechanism to induce low-angle grain boundaries. The dependency of yield stress on process parameters and alloy composition is quantitatively described.

* Corresponding authors.
E-mail addresses: fuhanwei@buaa.edu.cn (H. Fu), p.rivera1@lancaster.ac.uk (P.E.J. Rivera-Díaz-del-Castillo).

https://doi.org/10.1016/j.matdes.2021.110246
0264-1275/

1. Introduction

Laser powder bed fusion (LPBF) is an additive manufacturing (AM) technique; it is currently considered to be an alternative manufacturing route to conventional processes such as casting and forging [1]. Although it is generally accepted that due to higher cooling rates and finer microstructures, the mechanical properties of LPBFed alloys are superior than those of conventionally manufactured counterparts, the physical and mechanical behaviour of LPBF-built components are not yet well understood [2,3]. So far, the main focus of previous studies has been on controlling processing parameters to find windows to produce defect-free components, which can lead to superior mechanical properties compared with cast and wrought products [4–6]. However, even fully-dense LPBF samples that are produced with different processing parameters show wide ranges of mechanical properties [7]. Therefore, understanding the microstructural aspects that affect the mechanical properties of LPBF alloys can help to advance such technology.

It has been established that submicron cellular structures decorated with dense dislocation structures are one of the most unique features of LPBF alloys, and may have substantial impact on their strength [8–11]. Although extensive characterisation has been performed to unravel the complex nature of those structures, there is still debate on their origin, their influence on mechanical properties, and the methods to control their evolution so as to design microstructures with superior mechanical properties. Several mechanisms have previously been proposed for the formation of cellular structures: (i) constitutional stresses due to microsegregation [12], (ii) coherency strains due to precipitation networks [13], and (iii) the misorientation between dendrites that are accommodated by geometrically necessary dislocations [14]. Bertsch et al. [9] showed that none of these mechanisms can sufficiently explain the origin of cellular structures.

Bertsch et al. [9] suggested that there could be four main possible variables that control the formation of dislocation cellular structures: (i) cooling rate/strain rate during cooling, which determine the dendritic arm spacing; (ii) temperature gradients, which can determine the localisation of stress/strain during processing; (iii) hatch distance and layer thickness of the process, which can determine the number of heating/cooling cycles that a layer experiences during LPBF; (iv) the penetration of the melt pool to the substrate that can determine the characteristics of geometric constraints that are present around the newly deposited layers during processing. It can be concluded that residual stresses exceeding the yield strength of the material generate a plastic residual strain. This is imposed during LPBF due to repetitive thermal cycling, potentially having a substantial effect on the formation of dislocation cellular structures.

Dynamic recrystallization (DRX) and dynamic recovery (DRV) are thought to be some of the most important phenomena during thermo-mechanical processing of alloys, as they offer the possibility to control the desired microstructures after processing via grain refinement and dislocation density control [15]. LPBF undergoes several thermal cycles in which the material experiences several heating and cooling cycles; as a result of these, there is a tendency for the activation of DRX and DRV [7,16]. In a previous study, the authors showed that the compromise between dislocation multiplication and annihilation plays the most important role in controlling the yield strength of various alloys such as 316L stainless steel (SS), as well as nickel and titanium alloys in fully-dense conditions [7]. Thus, the study of DRX and DRV during LPBF is of particular importance. Depending on the thermo-mechanical processing conditions, two mechanisms are suggested for DRX in austenitic stainless steels: continuous and discontinuous dynamic recrystallization (CDRX and DDRX, respectively) [17]. CDRX is typically the main restoration mechanism at lower temperatures associated to the warm working region, but DDRX is often observed at higher temperatures known as the hot deformation region [18,19]. DRV acts as a perquisite for CDRX, as CDRX mechanism is based on the gradual increase in subboundary misorientations to become an actual grain boundary during the development of deformation [20]. The DDRX mechanism contains separate nucleation and growth processes of new grains in the highly dislocated (deformed) matrix [21]. It has been reported that grain refinement via CDRX can result in a combination of high yield and ultimate tensile strength in severe plastic deformation of steels [17,22,23]. However, there are no reports addressing this in LPBF. It is generally accepted that alloys with low to medium stacking fault energy undergo DDRX during thermo-mechanical processing at all temperatures and strain rate regions, although due to the large and complex thermal gradients involved in LPBF, this needs further clarification. The various mechanisms for the formation of cellular structures and new grains result in a complex microstructure; this is hierarchically arranged in solidification/dislocation cellular structures within subgrains that are formed in the actual grains.

A key strengthening mechanism in wrought components is the Hall–Petch effect [24]. It considers high-angle grain boundaries as effective barriers to dislocation movement. For alloys that undergo large deformations such as severe plastic deformation, a dislocation hardening term, based on a Taylor relationship, is added to the Hall–Petch contribution [25]. The same approach has been applied to LPBF-processed alloys to model their yield strength [26–29], although these approaches are not suitable from a process parameter optimisation point of view, as it is difficult to control both the grain size and dislocation density by changing the LPBF process parameters. Jia et al. [30] suggested a modified Hall–Petch relationship, which considers the combined effects of equiaxed and columnar grains in strengthening to model grain boundary strengthening. Wang *et al.* [10] correlated the solidification cellular structure size, known also as dislocation cell size (d_c, μm), to the yield strength of LPBF-produced 316L SS. They have derived the following Hall–Petch relationship between the yield strength (σ_Y, MPa) and d_c [10]:

$$\sigma_Y = 183.31 + \frac{253.66}{\sqrt{d_c}}. \quad (1)$$

However, Eq. (1) was obtained from wrought 316L SS data, relating the actual grain size to the yield strength. As the nature of dislocation cell walls, decorated with dense dislocation networks, differs from the irregular high-angle grain boundaries [31], the Hall–Petch coefficient 253.66 MPa$\sqrt{\text{m}}$ should be adjusted to incorporate dislocation cell strengthening. It is worth noting that the adoption of Eq. (1) for LPBF by Wang et al. was just applied to two specimens. Li *et al.* [11] further investigated the role of solidification/dislocation cellular size on yield strength of the LPBFed 316L SS using micropillar compression testing. They concluded that there is a weak dragging interaction between dislocations and cellular boundaries, and they suggested that the volume fraction of cellular boundaries, instead of their size, affects the yield strength. However, limitations such as a significant deviation of the strength values with the cell size (R^2=42%), as well as a narrow range of cell sizes that were covered in that study, may reduce the validity of the role of cell size in the strengthening of LPBF alloys.

Yanushkevich et al. [32] proposed a modified comprehensive Hall–Petch-type relationship to combine both the effects of actual grains and dislocation substructure contributions from wrought products. This approach is appropriate for alloy design and process parameter optimisation, because it only depends on the grain size

as a variable, which can be controlled via DRX and DRV during processing. However, there is not enough information to model the relationships between the dislocation cell size, grain size and dislocation density in LPBF processed alloys. LPBF processed alloys undergo complex microstructural transitions, which result in a large fraction of grains displaying low-angle boundaries. These substructures possess a higher dislocation density compared to the typical substructured grains from wrought products [33,34]. Thus, a grain boundary engineering approach is needed to clarify and quantify the role of low and high-angle grain boundaries in strengthening of LPBF alloys.

The aim of this study is twofold. Firstly, a new quantitative methodology is presented to shed light on the origins of the cellular structures, and the unique microstructural features of LPBF, using different modelling approaches. Secondly, a unified relationship is presented for the prediction of yield strength in LPBF alloys, considering the role of low- and high-angle grain boundaries. 316L stainless steel was selected as a typical representative of single-phase alloys without precipitation and phase transformations during LPBF processing. The specimens were produced with a wide heat input range in order to obtain a wide range of microstructures. The evolution of restoration mechanisms is modelled via Zener-Hollomon (classical) and the more recent thermostatistical approaches. Criteria to control restoration processes and maximise the yield strength by controlling both process parameters and alloy composition are suggested.

2. Experimental procedure, theory and modelling

2.1. Experimental methods

Pre-alloyed powder of chemical composition as shown in Table 1 was produced by gas atomisation with a particle size of 10–45 μm. To spread the range of heat inputs and grain boundary structures, the LPBF samples were produced in an argon atmosphere Renishaw plc (UK) AM125 with a laser spot size of 35 μm, and an AM125 machine with a laser spot size of 70 μm. Both machines were equipped with continuous wavelength lasers. The details for the 35 μm spot size specimen preparation have been reported in [4,34], including the associated characterisation. Flat tensile testing samples (for mechanical testing) and cubic (30 mm×30 mm×30 mm) samples (for microstructural characterisation) were fabricated using the process parameters shown in Table 2. A meander scanning strategy with 67° rotation at each layer was applied. To reduce the residual stresses, the powder bed in both machines was preheated to 80 °C. The corresponding heat inputs based on the normalised enthalpies (H_n) for each process parameters set are reported in Table 2. H_n can be calculated via [35]:

$$H_n = \frac{AP}{h_s\sqrt{\pi d v D^3}}, \quad (2)$$

where, A = 0.36 [4] is the absorptivity, P is the laser power, h_s=7.76×10^9 J/m^3 [36] is the enthalpy at melting temperature, d = 6×10^{-6} m^2/s is the thermal diffusivity, v is the laser scan speed and D is the laser spot size. If $H_n \geqslant 5.5$, evaporation occurs and keyhole pores can be formed during processing [4]. A wide range of heat inputs (4.5–6.6) is chosen to cover several microstructural evolution scenarios during LPBF.

Microstructural characterisation was performed on cross-sections of the cubic samples in the as-built state by optical microscopy (OM, Leica DFC295) and scanning electron microscopy (SEM) (Tescan Mira 3 LMHP field emission SEM) equipped with an electron backscattered diffraction (EBSD) detector (OXFORD Instruments Symmetry) at a scanning step size of 0.8 μm and an angular resolution of 0.1°. The OM micrographs were post-processed with ImageJ software [37] for porosity characterisation. The EBSD data were analysed using post-processing software HKL Channel 5. Room temperature uniaxial tensile tests were conducted in an Instron 3382 universal testing machine at an initial strain rate of 10^{-4} s^{-1}. For all 7 samples, 14 EBSD images were generated (2 per sample), all are uploaded in supplementary materials (Figs. S8-S14). Each EBSD map contained an average of ~1000 grains, so measurements reported on grain size are statistically representative. To reveal the solidification/dislocation cellular structure, transmission electron microscopy (TEM) was used. Disk specimens of 3 mm diameter were sectioned from the samples, and ground to a thickness of 50 μm, and then thinned using a Gatan 691 Type Ion Beam Thinner for TEM using TECNAI G20 operated at 200 kV.

2.2. Theory and modelling

2.2.1. Dynamic recovery and dynamic recrystallization background

The restoration mechanisms of DRV and DRX may occur during hot deformation of alloys, leading to enhancement of their formability at high temperatures. Their influence on the texture, grain size and morphology, make DRX and DRV key mechanisms for controlling the mechanical properties of wrought alloys [38]. These phenomena can also occur during creep, where a relatively low strain rate is applied [39]. LPBF is a process with inherent cyclic heating and cooling, where a relatively high strain rate results from quick contraction [34]. As a result, DRX and DRV can be activated when the thermo-mechanical conditions are appropriate. Examples of activation of DRX and DRV under ultra-high strain rates beyond 1000 s^{-1} can be found in [40,41]. Therefore, it is important to outline the most critical characteristics of DRX and DRV before introducing mathematical models to control and predict them.

In alloys where dislocation cross-slip and climb processes easily occur, DRV is the main restoration mechanism [42]. Deformation leads to an increase in the dislocation density, increasing the driving force for DRV [43]. Similar to the schematics Azarbarmas et al. [44] show in their work, the various restoration processes during thermo-mechanical processing are illustrated in Fig. 1. The occurence of DRV can be traced from microstructural characteristics such as the development of low-angle grain boundaries (LAGBs) and subgrains (Fig. 1a) [45]. In this work, the grains are categorised into two groups: (i) actual grains surrounded by high angle grain boundaries (HAGBs), Fig. 1c, centre panel; and (ii) subgrains that are surrounded by LAGBs, Fig. 1b, centre panel. It should be noted that subgrains themselves contain cells that are heavily dislocated (Fig. 1a). According to Humphreys [46], such subgrains carry high dislocation contents in their boundaries, which are LAGBs. Therefore, subgrains can play a vital role in the strengthening of alloys that underwent DRV.

When recovery processes occur at a slow rate during processing at high temperatures, DRX may take place once a critical strain/strain rate is reached [21]. DRX can be divided into two main

Table 1
Chemical composition of the powder in wt.%.

Fe	Cr	Ni	Mo	Mn	Si	P	S	N	C	Cu
Bal.	17.75	12.75	2.38	2	0.75	0.025	0.01	0.1	0.03	0.5

Table 2
Processing parameters including laser power (P), scan speed (v), layer thickness (t) and hatch distance (h) and the corresponding normalised enthalpies H_n used for LPBF processing. The sample set comprised 7 samples in total (supplementary material). For brevity, only the 4 samples with most variance in properties and process parameters are shown.

Sample	Laser spot size (μm)	P (W)	v (m/s)	t (μm)	h (μm)	H_n
S1	70	200	0.3	50	110	6.6
S2	70	200	0.45	50	110	5.5
S3	70	200	0.66	50	110	4.5
S4	35	100	1	20	70	5.1

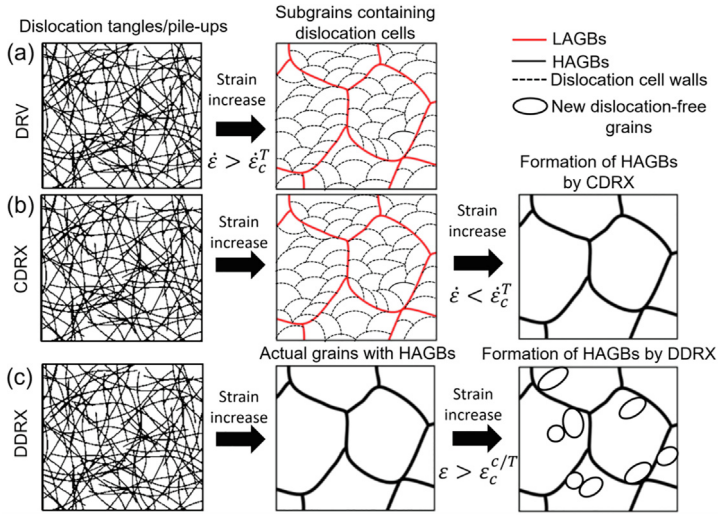

Fig. 1. Schematic description of restoration processes. (a) DRV, (b) CDRX, and (c) DDRX. Typically, the transition DRV→CDRX→DDRX occurs as temperature is increased.

mechanisms of CDRX and DDRX. If the subgrains developed during DRV processes rotate progressively and increase their misorientation angles due to the applied strain, HAGBs form and this mechanism is called CDRX, which is schematically shown in Fig. 1b [19,47]. Therefore, CDRX needs DRV as a prequisite. In fact, the increase in the HAGB fraction of the alloy is the result of the consumption of LAGBs as an overall strain energy minimisation process.

In contrast with CDRX, in which there is no clear distinction between nucleation and growth of the newly formed DRX grains, new grains (with HAGBs) developed by DDRX mechanism originate at the old deformed grain boundaries and thus, there is a clear distinction between the nucleation and growth stages [48]. The main microstructural characteristic of both DDRX and CDRX mechanisms is the development of HAGBs. However, unlike CDRX, new DDRX grains originate at the HAGBs of the deformed grains or old DRX grains (Fig. 1c, right panel). Therefore, the occurrence of DDRX does not lead to the consumption of LAGBs. The transition between CDRX and DDRX in an alloy is related to the concentration of solutes at the grain boundaries. If the boundaries are heavily loaded with solute, they cannot migrate quickly, which promotes the occurrence of CDRX against DDRX [49]. This can be an important factor in LPBF, as various process parameters lead to various cooling rates, which can induce solute segregation at grain boundaries. DRV, CDRX and DDRX feature strongly in the wrought alloys literature, but they are rarely associated to LPBF alloys [34]. The aim of this work is to show the impact of the various restoration mechanisms in controlling the mechanical properties of the LPBF 316L stainless steel, and provide a method to quantify them.

2.2.2. Modelling

Restoration mechanisms modelling can be performed within the frameworks of classical (Zener-Hollomon) and thermostatistical approaches. According to the classical approach, the critical strain (ϵ_c^c) for the activation of DDRX in 316L SS can be estimated from [50]:

$$\epsilon_c^c = 0.009Z^{0.084}, \tag{3}$$

where Z is the Zener-Hollomon parameter. $Z = \dot{\epsilon}\exp(\frac{Q}{RT})$, where $\dot{\epsilon}$ is the process strain rate, Q = 460 kJ/mol [51] is the activation energy for triggering DRX in 316L SS, R = 8.314 J/mol·K is the universal gas constant and T is the processing temperature. $\dot{\epsilon}$ for LPBF processing can be calculated via [7]:

$$\dot{\epsilon} = \frac{kT_{peak}v}{P}, \tag{4}$$

where k = 29 W/m·K [52] is the thermal conductivity and T_{peak} is the process peak temperature. T_{peak} can be estimated via [7]:

$$T_{peak} = \frac{H_n T_b}{H_n^{max}}, \tag{5}$$

where T_b=2885 K is the boiling temperature and H_n^{max}=5.5 is the maximum allowable heat input before the onset of evaporation.

According to the thermostatistical approach, the critical strain, ϵ_c^T for the activation of DDRX can be estimated via [53]:

$$\epsilon_c^T = \frac{\frac{1}{2}\mu b^3 - \left(1+\frac{1}{k_c}\right)T\Delta S}{\frac{1}{2}\mu b^3}, \tag{6}$$

where μ=74×10^9 Pa [54] is the shear modulus, b = 2.54×10^{-10} m [55] is the magnitude of the Burgers vector, ΔS is the statistical entropy of dislocations and $k_c = \frac{12\pi(1-\nu)}{(2+\nu)}\left(1+\frac{T\Delta S}{\mu b^3}\right)$ [53], where ν=0.3 is the Poisson ratio. The dislocation statistical entropy can be calculated via:

$$\Delta S = k_B \ln\left(\frac{\dot{\epsilon_0} + \vartheta}{\dot{\epsilon}}\right), \tag{7}$$

where k_B=1.38×10^{-23} J/K is the Boltzmann constant, $\dot{\epsilon_0} = cb\rho_Y$ is a limiting strain rate related to the speed of sound (c = 5280 m/s [56]), and ρ_Y is the dislocation density at the yield point ($\rho_Y = (0.9\sigma_Y/\mu b)^2$), where σ_Y is the material's yield strength [53]); $\vartheta = 10^{13}\exp\left(-\frac{E_m}{RT}\right)$ is the frequency of atomic jump of vacancies and E_m=73.12×10^3 J/mol is the vacancy migration energy.

In addition to DDRX prediction, the thermostatistical theory also predicts the possibility of activation of CDRX and DRV via the critical processing strain rate ($\dot{\epsilon_c}^T$) [57]:

$$\dot{\epsilon}_c^T = (\dot{\epsilon_0} + \vartheta)\exp\left(-\frac{\frac{\lambda}{2}\mu b^3 - \frac{2xl^*}{bk_c}\Delta G_{sys}}{k_B T}\right), \tag{8}$$

where λ=0.6 [57] is a length scaling constant, x is the solute concentration in molar fraction ($0 \leqslant x < 0.5$), $l^* = 12.5b$ is the dislocation's distortion length, which accounts for 98% of the total strain field induced by dislocations and ΔG_{sys} is the Gibbs free energy of the alloy, representing the energy barrier accounting for the possible atomic arrangements in the lattice. Expressions for various alloy grades can be found in [57]. If $\dot{\epsilon} < \dot{\epsilon}_c^T$, then CDRX takes palce. Otherwise, DRV is the main restoration process [57].

3. Results

3.1. Microstructure of as-built specimens

3.1.1. Grain characteristics and porosity measurements

EBSD inverse pole figure (IPF) maps of 316L SS after LPBF processed with different parameters were taken from the centre of the cubic samples and from the grip of the tensile testing samples are shown in Fig. 2. S1-S4 (Table 2) displayed fine grains without preferred orientation; this is a selection of the seven builds displaying most variance in microstructure and properties. As displayed by EBSD, the average grain size (GS) is determined using the average grain area method, considering both high- and low-angle grain boundaries (HAGBs and LAGBs, respectively) respectively for S1, S2, S3 and S4 is 11.2±5.0, 6±4.0, 5.3±4.0, and 4.7±2.0 μm. Grains with low-angle boundaries (subgrains) are considered in reporting the average grain size, due to their significant role in strengthening. The actual grain size of the samples (d_G), considering only HAGBs are 22±5, 35±2, 20±9, and 35±9 μm for S1, S2, S3, and S4, respectively. The respective aspect ratio (AR) is 1.8, 2, 2 and 2.45. This indicates that S1-S3 are more homogeneous and S4 experienced a more inhomogeneous grain refinement process.

As porosity is known to influence the microstructural evolution and mechanical properties of LPBF-processed parts [58,4], representative as-polished OM black and white contrast images for S1-S4 are shown in Fig. 3. A thorough statistical analysis has been done to measure the density of the as-built samples using at least 18 OM images (see supplementary materials, Figs. S1-S7) per sample. S1 has been processed with H_n=6.6, which exceeds H_n^{max}, leading to keyhole formation, as shown in Fig. 3a. Irregularly-shaped pores, which can be lack-of-fusion regions, are also evident; the average porosity content of S1 is 0.89±0.2 %. S2 and S3 are processed with H_n <5.5, therefore, there are quite a few spherical pores present. The most prevalent type of pore in S2 and S3 is lack of fusion and the density of pores is 0.62±0.2% and 2.25±0.3% for S2 and S3, respectively. S4 was produced based on an optimisation of the process parameters methodology presented in [4], and the density of pores in this sample was 0.03 ±0.01%. S1 to S4 specimens do not intend to relate porosity to mechanical properties, but rather heat input to the restoration mechanisms introduced in Section 2.2.1.

3.1.2. Dynamic recrystallization features

Fig. 4 shows representative images of the recrystallization maps of the LPBF-processed samples before tensile testing. The grains can be categorised as deformed, substructured and recrystallized. HKL Channel 5 software takes each grain and measures its internal average misorientation angle. If the average misorientation angle within a grain exceeds the angle threshold of 2°, the grain is classified as deformed. Grains that contain subgrains whose internal misorientation is under 2° but the misorientation across subgrains is above 2° are classified as substructured. The remaining grains, which contain subgrains of misorientations under 2°, and misorientation across subgrains being under 2° are categorised as recrystallized. It is worth noting that these definitions of deformed, substructured and recrystallized are widespread in the literature. A range of authors producing well-established work have adopted them [59–63].

In Fig. 4, the blue areas represent recrystallized grains, which are distributed non-uniformly across the samples. It can be seen that the recrystallization fraction is more pronounced in S2 and S3, compared with S1 and S4 (Table 3). Conversely, the deformed

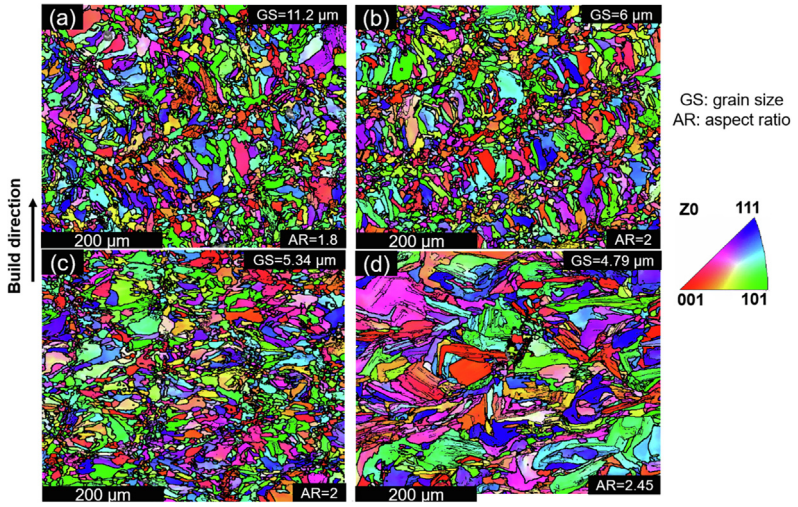

Fig. 2. EBSD IPF maps of 316L SS built with different process parameters: (a) S1, (b) S2, (c) S3 and (d) S4.

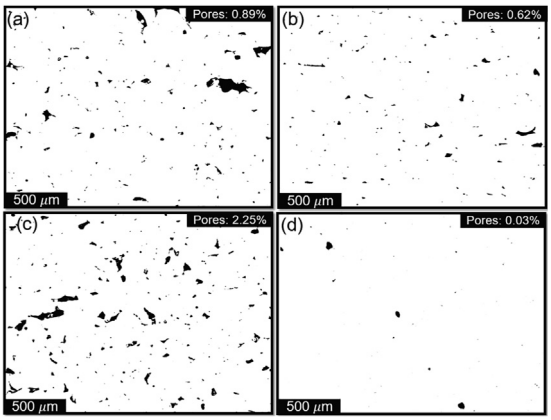

Fig. 3. Black and white contrast of as-polished OM images of the samples (a) S1, (b) S2, (c) S3 and (d) S4, processed by ImageJ software.

grains (red in Fig. 4) fraction is quite high in S4 and S1, in comparison with S2 and S3. The recrystallized, substructured (yellow in Fig. 4) and deformed fractions were obtained for each sample from EBSD post-processing, and are shown in Table 3. S3 and S2 possess the highest recrystallization fractions with 0.16 and 0.12, respectively, and they also have the lowest deformed grain fractions. S4 and S1 have the highest deformed grains fraction with 0.36 and 0.23, respectively, as well as the lowest recrystllized fraction. Substructured grains, which can be attributed to the grains that underwent DRV, have almost the same fraction in S1-S3 (∼0.7), however, their fraction is lower in S4 (0.59). This indicates a significant contribution of restoration mechanisms during LPBF of 316L SS, which resulted in grain refinement in all samples.

Fig. 5a-c show that samples S1-S3 possess a large fraction of HAGBs ($\geqslant 15°$), approximately 0.55–0.62 of the total. Conversely, Fig. 5d shows that S4 has a large fraction of LAGBs ($<15°$), 70% of the total. The fractions of LAGBs and HAGBs for all samples are presented in Table 4. The microstructures of all samples also display numerous incomplete LAGBs (indicated by arrows in Fig. 5) inside the grains with HAGBs, which is a feature of CDRX [18,32]. It can be seen that the incomplete grain boundaries are frequent in S4. Generally, such a wide distribution of LAGBs and HAGBs fraction are characteristic of DRX structures [64]. Comparing Figs. 4d and 5d shows that most of the deformed grains contain a high density of substructures (LAGBs), which contribute significantly to the strengthening of S4. Such LAGBs can be seen in S1-S3 (Figs. 5a-c), but to a much lower extent.

Face-centred cubic (FCC) alloys tend to generate twins during thermo-mechanical processing [65]. Fig. 6 shows the distribution of Σ3 boundaries (twin boundaries) in the as-built samples. In S1-S3, severe twinning occurred during processing (∼0.12–0.14 of the total boundaries). However, the presence of twins is negligible in S4. The fraction of twin boundaries is presented in Table 4. In S1-S3 samples, the twins were not distributed uniformly; they were observed mainly in the recrystallized regions and fine deformed areas (Figs. 6a-c). The formation of such high number of twins and large fractions of HAGBs during LPBF in samples S1-S3, as well as the absence of twin boundaries and evolution of large fraction of LAGBs in S4 can be attributed to the various DRX mechanisms activated during LPBF of 316L SS.

3.1.3. Cellular structures

Solidification/dislocation cellular structures are typical features of LPBF alloys [66,31,10,67]. In S1-S4, the average size of the cellular structure was in the submicrometre scale, and varied with process parameters (Fig. 7). Fig. 7 shows a relatively high density of dislocations on cell walls, in contrast with the relatively low density in their interior. During LPBF, solidification characteristics such as thermal gradients and cooling rate can determine the size and wall thickness of the solidification cells [68]. Average dislocation cell size (d_c) values for different samples are listed in Table 5; a series of TEM images were used to measure the average cell size including a minimum of 50 measurements per sample. Due to microstructural scatter, TEM imaging could not be adopted to quantify dislocation density.

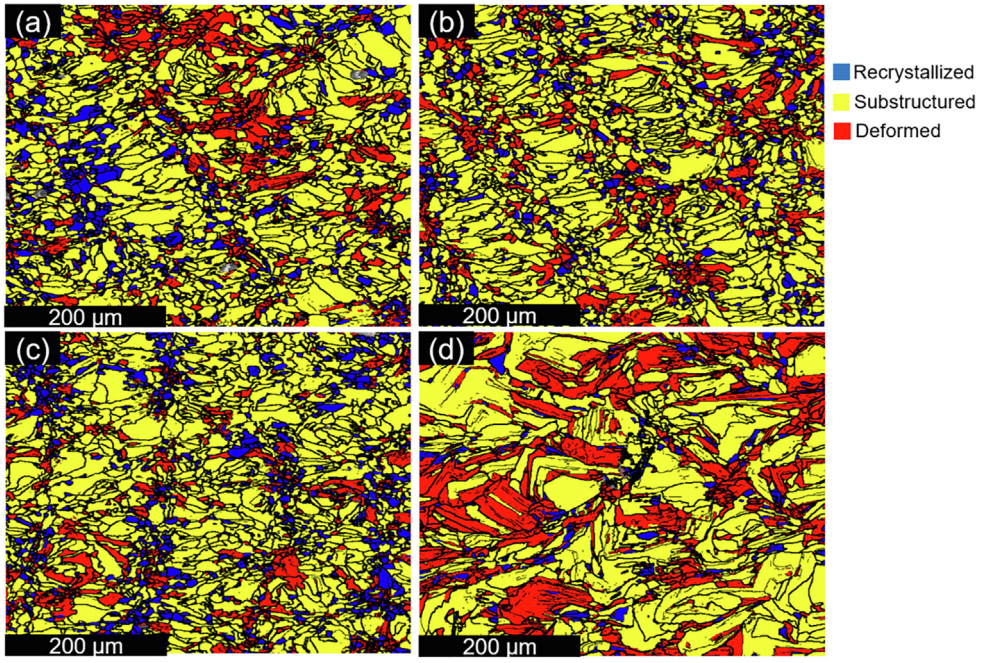

Fig. 4. Recrystallization maps of the as-built samples: (a) S1; (b) S2; (c) S3 and (d) S4. Blue, yellow and red areas represent recrystallized, substructured and deformed grains, respectively.

Table 3
Fractions of recrystallized, substructured and deformed grains, derived from EBSD analysis.

Sample	Recrystallized	Substructured	Deformed
S1	0.07±0.02	0.7±0.02	0.23±0.02
S2	0.12±0.01	0.69±0.03	0.19±0.02
S3	0.16±0.02	0.69±0.02	0.15±0.02
S4	0.05±0.01	0.59±0.03	0.36±0.02

According to Bertsch et al. [9] if the average primary dendrite arm spacing is similar to the size of dislocation cellular structures, it can be concluded that dendrites and dislocation cells may overlap. The primary dendrite arm spacing, measured from representative SEM images of S1-S3, which is shown in Fig. 8 (Note that S4 was not available for this study). The average dendrite arm spacing is also reported in Table 5. It can be seen that d_c and primary dendrite arm spacing size are quite similar, suggesting the formation of dislocation cellular structures on the dendritic structure caused by solidification. The view adopted in this work is that the thermo-mechanical cycling underwent by the build in LPBF will impose localised cyclic strains that are not experienced by wrought alloys. Such strains may partially restore the crystallinity at the dendrite interfaces; high temperatures combined with a quick reorientation of the structure may realign otherwise disordered interfaces. Strain relaxation in subsequent cycles may be achieved through the formation of low energy dislocation structures, i.e. dislocation cells. This is schematically shown in Fig. 9.

In addition to dislocation cells, deformation nanotwins are observed in Fig. 7b. Those features are observed in all the samples. The details of the formation of nanotwins and their roles in strengthening and micrsotructural evolution is the subject of an upcoming publication.

3.2. Mechanical properties

Tensile testing was performed on as-built samples perpendicular to the build direction with flat geometry. Representative stress–strain curves of the as-built samples are displayed in Fig. 10a. Mechanical property values are listed in Table 6. Yield strength (YS) and ultimate tensile strength (UTS) of the specimens strongly depend on the process parameters. Fig. 10b compares the present results with conventional manufacturing. A dataset comprising as-cast, wrought and hot-rolled 316L SS [69] is presented; it is shown that the spread in mechanical properties such as YS and elongation is increased for the samples produced in this work. This shows that even little changes in process parameters such as the scan speed (in S1-3) can lead to large YS and elongation variations. The specimen with the lowest porosity and recrystallized fraction showed highest YS and UTS. However, there is no clear correlation between the YS and the UTS of the samples with porosity content, as S1 with 0.89±0.2% porosity has a quite higher YS than S2 with only 0.62±0.2% porosity. This shows the significance of the influence of microstructure development on YS and UTS of LPBF-processed 316L SS. This is in agreement with the recent findings on the link between mechanical properties and porosity content [70,71]. Ronnenberg et al. [70] showed that the presence of pores has no effect on the yield strengthening of LPBF 316L SS, as they found out that two specimens with the same porosity contents undergo yield at different stress values. YS is controlled only by microstructural features such as grains and grain boundaries, and solidification characteristics. They further showed that only ductility and failure mechanisms can be affected by lack-of-fusion porosity. The fact that YS is not related to porosity content is also statistically proved by Jost *et al.* [71]. After the investigation of 75 LPBF as-built 316L SS samples as a function of pore size, size distribution, and morphology, they concluded that only ductility and strain at the ultimate tensile strain are affected by the presence of pores. They showed that the critical pore size beyond which ductility can be affected is about 125 μm. It can be seen that YS and UTS increase with a decrease in the recrystallized fraction and an increase in the deformed fraction in the processed samples (Tables 3 and 6).

There is also a correlation between LAGBs fraction and strength levels, as strength increases with an increase in LAGB fraction. Interestingly, ductility values are not affected by the porosity

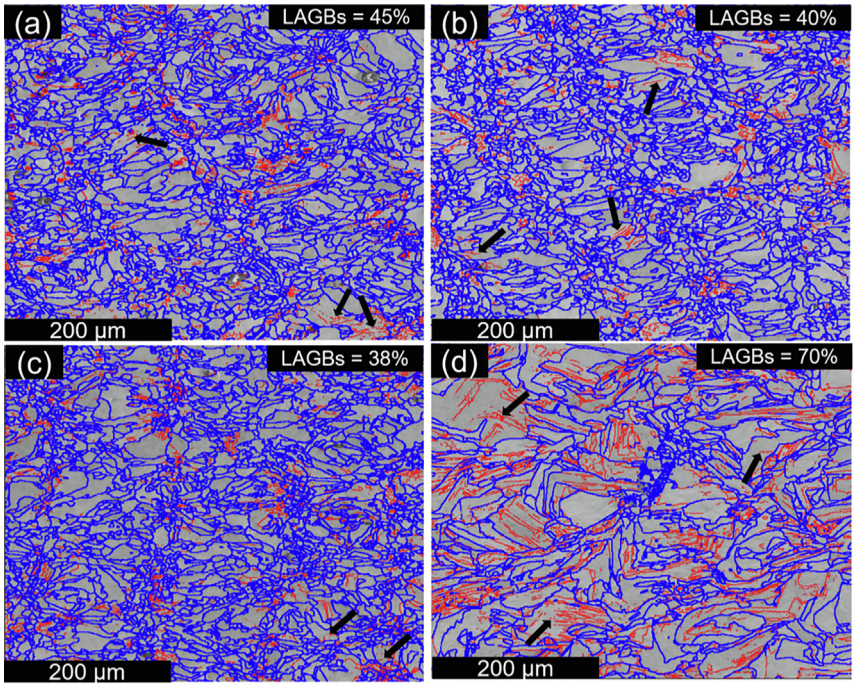

Fig. 5. LAGB and HAGB maps of (a) S1, (b) S2, (c) S3 and (d) S4, LAGBs (<15°) are coloured red and HAGBs (⩾15°) are coloured blue.

Table 4
Fraction of LAGBs, HAGBs and twin boundaries of the as-built samples with various process parameters.

Sample	LAGBs	HAGBs	Twin boundaries
S1	0.45	0.55	0.12
S2	0.4	0.6	0.14
S3	0.38	0.62	0.14
S4	0.7	0.3	0.02

content in these samples, as S1 and S2 have quite higher elongation to failure levels than the fully-dense S4. This may be due to the small pore size that is present in the samples. Statistical analysis showed that more than 90% of the pores in S1-S4 have a size under 125 μm, which is known as the critical pore size to trigger mechanical properties deterioration [71]. The observation of large variations in mechanical properties for samples printed with a small variance in scan speed (S1-S3), as well as the lack of correlation between mechanical properties and porosity contents, points to the possibility of controlling mechanical properties by optimising microstructural evolution, e.g. the LAGB structure. The authors have also recently shown that even utilising optimised process parameters to produce fully-dense 316L SS with LPBF can lead to a large variation in mechanical properties [7]. Both porosity and microstructure optimisation have been performed for S4 and the highest YS and UTS are achieved.

S1 and S2 showed the best tensile ductility (54% and 56%, respecively). Strengthening in S4 is accompanied by a degradation in ductility, despite the fact that S4 has been produced with almost no porosity, but S1 and S2 contain dense pore structures (Figs. 3a and 3b). Improved elongation in S1 and S2 cannot be correlated to porosity, in contrast to previous reports on the significance of porosity contents on ductility [72,73]. S3 shows the poorest ductility and YS. In this special case, it can be conjectured that large

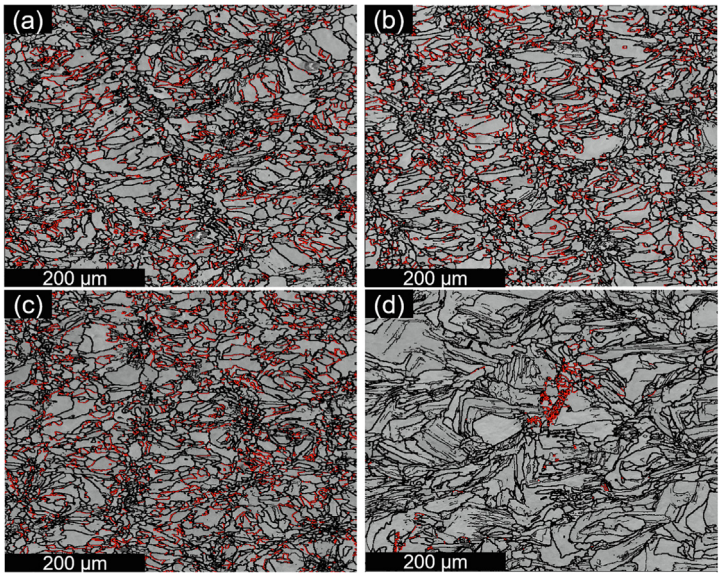

Fig. 6. Grain boundary maps showing the distribution of twins (red boundaries) in (a) S1, (b) S2, (c) S3 and (d) S4.

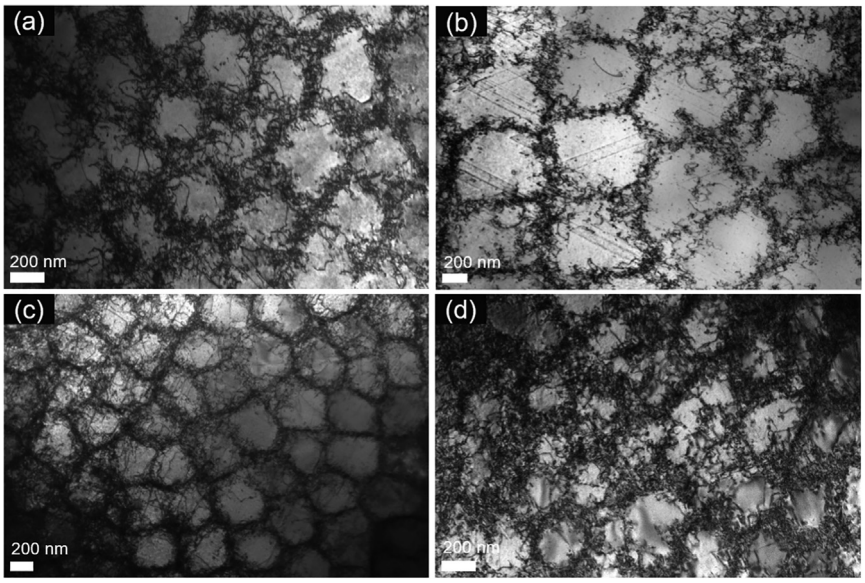

Fig. 7. Representative bright field TEM images showing dislocation cellular structures in (a) S1, (b) S2, (c) S3 and (d) S4.

porosity contents (mainly lack of fusion) of about 2% (Fig. 3c) may affect the plasticity mechanisms negatively, although further modelling and characterisation efforts are required to confirm this, which is not in the scope of this research.

3.3. Restoration mechanisms analysis

3.3.1. Thermal model

In order to model restoration mechanisms as the main effective microstructural developlemt phenomenon, temperature gradients (G [K/mm]) during processing for all samples are determined via an empirical thermal model developed by Bertoli et al. [67]:

$$G = 10570\left(\frac{P}{v}\right)^{-0.42}. \quad (9)$$

Eq. (9) indicates that the temperature variations due to laser penetration are significantly dependent on scan speed. Even a little change of the scan speed from 0.3 m/s (S1) to 0.45 m/s (S2) can cause a significant difference of 1.25×10^4 K/mm to 1.48×10^4 K/mm, (about 18% change) in the temperature gradient. Eq. (9) is a first attempt to estimate temperature gradients during LPBF of 316L SS. This empirical equation can be modified and improved to also consider the effects of laser machine characteristics such as laser profile, and spot size, as well as the presence and direction of the gas inside the chamber, which may influence temperature gradients. However, the applicability of Eq. (9) in this work is reliable, because the only difference between two LPBF machines used in this study is the laser spot size, which effect on the heat input is taken into account through the normalised enthalpy (Eq. (2)).

The temperature–time profiles of samples processed with different parameters follows a method reported by the authors earlier [34]; the temperature decay during layering should be determined.

Table 5
Average dislocation cellular structure size and the average primary dendrite arm spacing of the LPBF as-built 316L SS samples.

Sample	d_c (μm)	dendrite arm spacing (μm)
S1	0.33±0.05	0.45±0.04
S2	0.59±0.10	0.62±0.02
S3	0.34±0.04	0.38±0.07
S4	0.40±0.08	-

A schematic of LPBF process is shown in Fig. 11a (the schematic of the process is adapted from [74]). The build has been split into cubes to highlight the impact of layer thickness and hatch distance. When the laser begins to interact with the powder bed/building part at point a (melting begins at the layer), temperature rises to T_{peak}, which can be estimated via Eq. (5). Depending on the scan speed, the laser moves at a certain time to point b in the $-x$ direction, which magnitude is determined by the hatch distance and this is repeated until a layer is formed. The laser then moves in the $-z$ direction a layer thickness. When this happens, the temperature decay at the point b can be estimated by multiplying the hatch distance by the temperature gradient:

$$\Delta = G \times h. \quad (10)$$

When the second layer is deposited, the temperature in the previous layer (first layer) drops to a value of $T = T_{peak} - \Delta$. Similar to this, the temperature at the point c can be estimated by multiplying the layer thickness by the temperature gradient:

$$\delta = G \times t. \quad (11)$$

Thus, the maximum temperature during the deposition of the second layer has a value of $T_{peak} - \delta$. This pattern is repeated for the deposition of the next layers and the relevant temperature–time profiles that each layer experiences during LPBF for different samples are plotted in Fig. 11b. Each of the temperature rises and drops in Fig. 11b is known as a thermal cycle. It is assumed that when $T_{peak} - \Delta \leqslant T_0$, the minimum temperature of the melt pool is the same as the previous thermal cycle, where T_0 is the powder bed temperature. The corresponding time during layering can be estimated by the reciprocal of the strain rate ($1/\dot{\epsilon}$), where $\dot{\epsilon}$ at each thermal cycle is determined via Eq. (4). Fig. 11b shows that the samples experience quite different thermo-mechanical processing schemes during LPBF, which depend on the process parameters. The deposited layers in S1 experience three consecutive rapid melting and two rapid solidification processes during LPBF. They also undergo two thermal cycles at temperatures that are prone to DRX and DRV (shown in red and green circles, respectively, in Fig. 11b). It is generally accepted that metallic alloys that are processed at temperatures above $0.8T_m$ and $0.5T_m$, where T_m is the melting temperature, are prone to DRX and DRV, respectively [15]. Layers in S2 and S4 experience only two fast melting and solidification stages. Both of them undergo DRX at the third thermal cycle, but only S4 is prone to DRV at the fourth thermal cycle, while

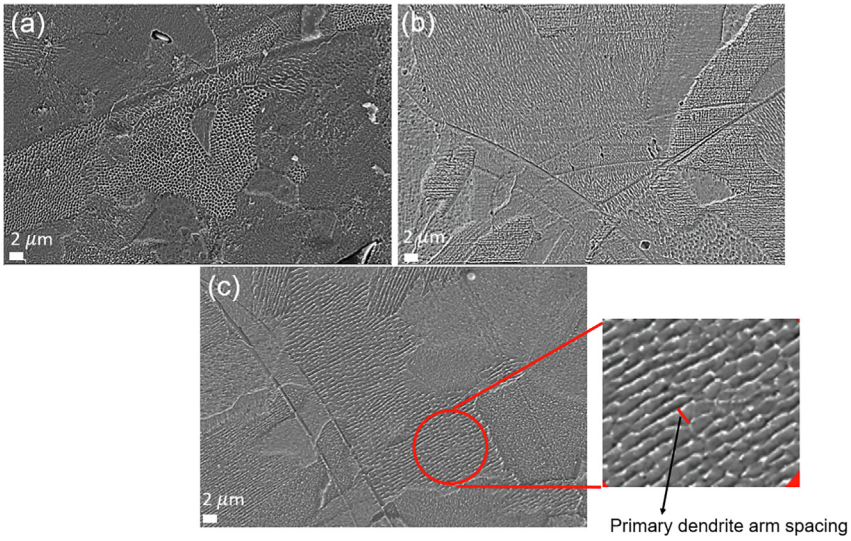

Fig. 8. Representative SEM micrographs showing primary dendrite arm spacing in the LPBF as-built samples. (a) S1, (b) S2, and (c) S3.

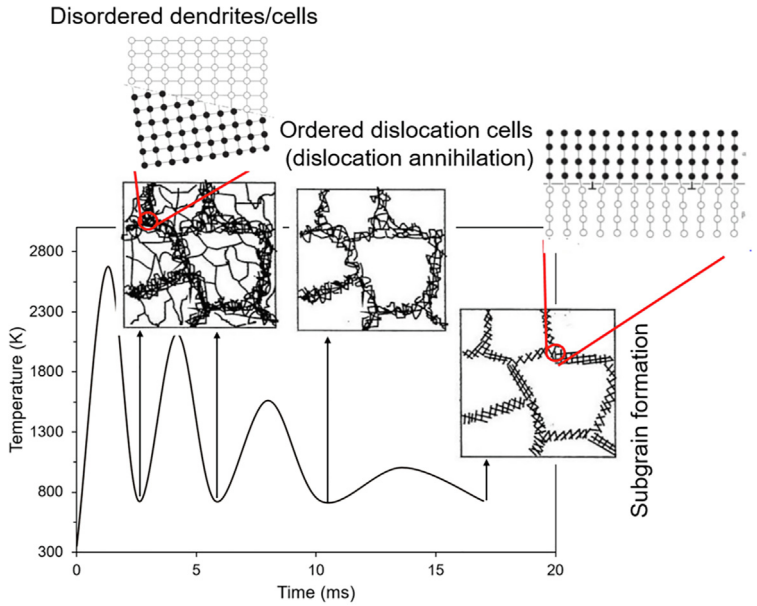

Fig. 9. Schematic showing dislocation rearrangement on cells/dendrites as a result of thermo-mechanical processing in LPBF, leading to subgrain formation.

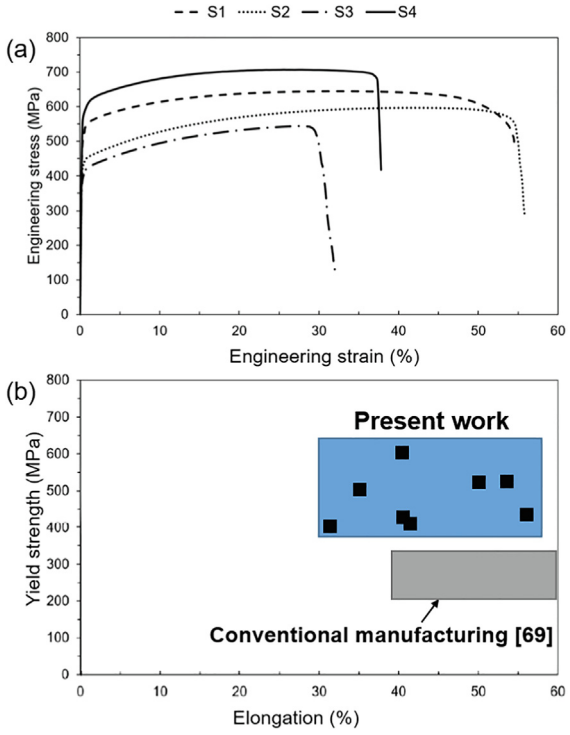

Fig. 10. (a) Representative engineering tensile stress–strain curves of the as-built samples. (b) Comparison of the yield strength and elongation values of samples produced with LPBF in this work and conventional manufacturing (as-cast, wrought, and hot rolled 316L SS). Present work values are listed in Table 6 and Table 10.

DRV cannot take place in the fourth cycle in S2. S3 layers just experience two thermal cycles during LPBF, which can be related to rapid melting/solidification and DRX.

3.3.2. Thermal and plastic strains

In order to predict what restoration mechanisms are active during the LPBF of different samples, the thermal and plastic strains induced during LPBF should be estimated. The thermal strain

Table 6
Mechanical properties of the as-built samples.

Sample	Yield strength (MPa)	Ultimate tensile strength (MPa)	Elongation (%)
S1	518±1	644±14	54±4
S2	432±16	596±7	56±6
S3	400±16	543±15	32±3
S4	600±5	707±7	38±1

(ϵ_T), which is induced as a result of repetitive expansion and contraction during heating and cooling cycles, can be estimated via:

$$\epsilon_T = \sum_i \alpha_{CTE} \Delta T_i, \tag{12}$$

where α_{CTE}=20.21×10^{-6} K^{-1} [52] is the coefficient of thermal expansion and ΔT_i is the difference between the peak temperature at each heating/cooling thermal cycle and its corresponding minimum temperature. ϵ_T for different samples are listed in Table 7. It should be noted that thermal strain is not residual, just influencing microstructural evolution throughout the layering process.

To estimate the accumulated plastic residual strain induced by deformation during LPBF processing, hardness values of the samples are correlated with the strain, based on measurements from laser welding [75]. Elmesalamy et al. [75] showed that in laser welding, only the welding scan strategy, and the thermo-mechanical cycles inherent to the process influence the accumulated residual plastic stress/strain. In their research, they ignored the effects of solidification-related microstructures such as the size and morphology of cellular structures or columnar grains. Due to the similar physics of laser welding and LPBF, their approach has been used in this study to estimate the plastic residual strain induced by LPBF processing. Oliveira *et al.* [76] also correlated the effects of laser on microstructure and phase transformations of NiTi alloy in both laser welding and AM. They showed that the thermal variation similarities between laser welding and AM paves the way to using modelling approaches from laser welding in AM. The correlation between the hardness and the plastic residual strain in laser welding, which is estimated by Elmesalamy *et al.* [75], is shown in Fig. 12. The measured hardness values for S1, S2, S3 and S4 are 192±5 HV, 195±6 HV, 186±12 HV and 237±5

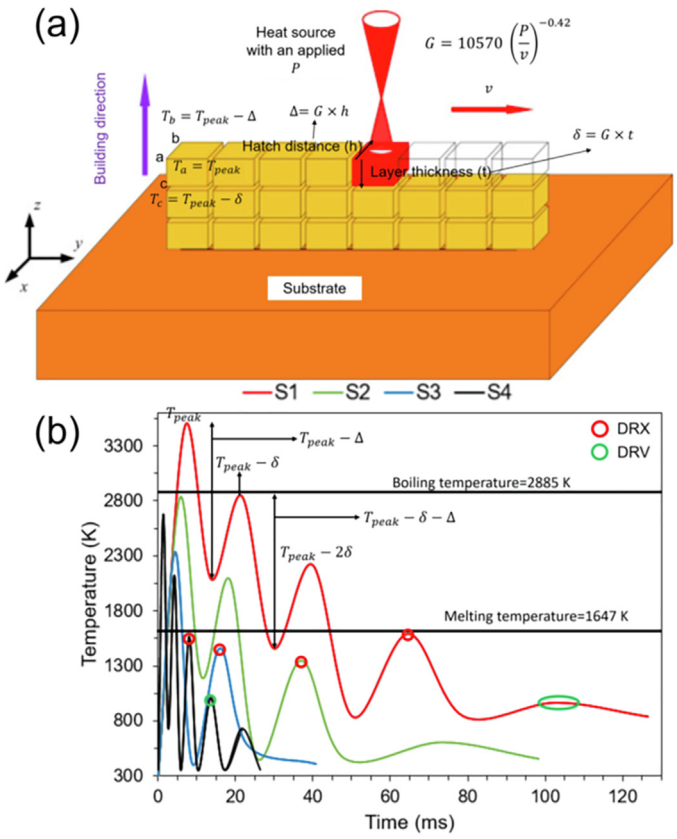

Fig. 11. (a) A schematic of LPBF showing how the thermal model is applied. (b) Temperature–time profiles showing thermal cycles that a layer experiences during LPBF of different samples. Time is calculated as the reciprocal of the strain rate ($1/\dot{\epsilon}$). The temperatures in which the material is prone to DRX and DRV are shown in red and green circles, respectively.

HV, respectively (shown in Fig. 12). A comparison between the measured hardness values and d_c values for different samples (Table 5) shows that there is no correlation between the solidification cellular structures size and hardness, which validates the adoption of the approach from laser welding in the current form for our study. The corresponding ϵ_p for each sample is shown in Fig. 12 and listed in Table 7. Thus, the total strain induced by LPBF is $\epsilon_t = (\epsilon_T + \epsilon_p)$, which is also listed in Table 7.

3.3.3. DRX and DRV activation

To predict DDRX activation, two methods are employed: classical (Zener-Hollomon) and thermostatistical approaches. Based on temperature–time profiles (Fig. 11b) a summary of the phenomena activated at each thermal cycle during layering of each sample is listed in Table 8. The thermal cycles prone to DRX and their respective $\dot{\epsilon}$ and temperatures are indicated in Fig. 11b and Table 8. These yield Z values of 8.22×10^{16} s^{-1}, 5.54×10^{19} s^{-1}, 3.71×10^{18} s^{-1} and 10^{18} s^{-1} for S1, S2, S3 and S4, respectively. Using Eq. (3), the ϵ_c^c for the activation of DDRX is estimated and listed in Table 7.

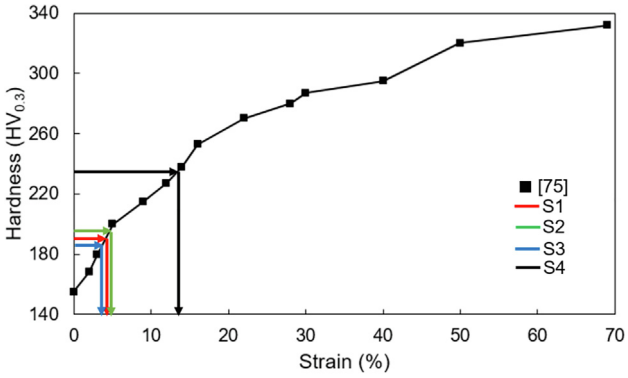

Fig. 12. Correlation between the hardness and the residual plastic strain adopted from laser welding [75].

According to this approach, only S1 and S4 are prone to DDRX, as their corresponding $\epsilon_t \geqslant \epsilon_c^c$.

Interestingly, the thermostatistical theory yields very similar values to the classical theory for ϵ_c of DDRX. The corresponding ϵ_c^T for all samples is also listed in Table 7. This approach suggests that only S4 is prone to DDRX. Therefore, it can be concluded that DDRX is an active mechanism in S4. S1 may experience DDRX to some extent. But, S2 and S3 have not experienced DDRX during LPBF.

To examine the possibility of CDRX activation during LPBF, the thermostatistical approach is used. The $\dot{\epsilon}_c^T$ for the activation of CDRX can be estimated via Eq. (8). To calculate $\dot{\epsilon}_c^T, \Delta G_{sys}$ (kJ/mol) is estimated via [57]:

$$\Delta G_{sys} = -(1.69 + 0.013T + 3.1\times10^{-5}T^2), \quad (13)$$

where T is taken as the peak temperature for each thermal cycle (Fig. 11b). $\dot{\epsilon}_c^T$ for the thermal cycles that the material is prone to DRX is calculated and compared with the relevant $\dot{\epsilon}$ at that thermal cycle in Table 9. It can be seen that $\dot{\epsilon}$ is not enough to activate DRV at the corresponding thermal cycles that is recognised as the material is prone to DRX. This means that CDRX occurs readily at those thermal cycles in S1-3. However, in S4, the $\dot{\epsilon}$ is almost the same as the $\dot{\epsilon}_c^T$, which means that CDRX is not activated in S4. In other words, the thermo-mechanical conditions in the third thermal cycle of the S4 leads to occurrence of DRV, but in contrast to S1-S3, the driving force is not enough so that those dynamically recovered grains act as promoters for CDRX. As is mentioned in the previous sections, DRV acts as a prequisite for occurence of CDRX, but if the strain rate is high enough, CDRX cannot be activated.

4. Discussion

The microstructural evolution of 316L austenitic SS processed by LPBF is governed by the activation of DRX and DRV. Thermal cycles containing rapid solidification/melting (Fig. 11b) in all samples result in the formation of a highly dislocated (deformed) microstructure with a dendritic structure. This provides the necessary stored energy for the activation of restoration mechanisms

Table 7
Thermal, plastic and total strain induced by LPBF of 316L SS. Critical strain for DDRX are estimated via both classical (ϵ_c^c) and thermostatistical (ϵ_c^T) approaches.

Sample	ϵ_T	ϵ_p	ϵ_t	ϵ_c^c (Eq. 3)	ϵ_c^T (Eq. 6)
S1	0.19	0.05	0.24	0.24	0.26
S2	0.17	0.06	0.23	0.4	0.42
S3	0.12	0.04	0.16	0.32	0.34
S4	0.18	0.14	0.32	0.29	0.31

Table 8
Phenomena activated during various thermal cycles (Fig. 11b) in each layer in the studied samples. RM and RM/S represent the rapid melting and rapid melting/solidification, respectively.

Sample	1st cycle	2nd cycle	3rd cycle	4th cycle	5th cycle
S1	RM	RM/S	RM/S	DRX ($\dot{\epsilon}$=69 s^{-1}, T = 1594 K)	DRV
S2	RM/S	RM/S	DRX ($\dot{\epsilon}$=88 s^{-1}, T = 1350 K)	Deformation	-
S3	RM/S	DRX ($\dot{\epsilon}$=140 s^{-1}, T = 1463 K)	-	-	-
S4	RM/S	RM/S	DRX ($\dot{\epsilon}$=454 s^{-1}, T = 1563 K)	DRV	-

Table 9
Critical strain rate (s^{-1}) for the activation of DRV/CDRX mechanisms during processing at the relevant thermal cycles of different samples. The applied process strain rates are also reported.

Sample	$\dot{\epsilon}_c^T$ at thermal cycle prone to DRX	$\dot{\epsilon}$ at the corresponding cycle
S1	495	69
S2	400	88
S3	445	140
S4	455	454

during subsequent thermal cycles during LPBF. When a medium stacking fault energy alloy such as 316L SS deforms, dislocations typically arrange in the form of cell structures [46]. During the rapid solidification/melting thermal cycles of LPBF, the material experiences large strains, which can resemble shock-loaded materials. Therefore, dislocations arrange themselves on primary dendrite arms in the form of cell structures with the walls being complex dislocation tangles. When DRV occurs in the subsequent thermal cycles, either as a distinct process, or as a prerequisite for CDRX, the dislocation tangles in cell walls become more organised and form regular dislocation networks or LAGBs. Subsequently, the number of dislocations in the cell interiors decreases with a progress in recovery. As a result, the cells become subgrains bordered by LAGBs. The transition from dislocation cells to LAGBs involves annihilation of redundant dislocations and rearrangement of the rest into LAGBs. The transition from cellular structures to subgrains can be suppressed in alloys, in which DRX extensively occurs. This is the reason why more LAGBs are formed in S4, compared to other alloys, because in S1-S3 the critical strain rate for the activation of DRV is not reached, and CDRX occurs readily during their DRX cycle.

Thermal cycles prone to DRX (red circles in Fig. 11b) experience different mechanisms. In S1-S3, CDRX is the dominant mechanism, whereas DDRX is activated in S4. DRV is believed to be the main assistance for the activation of CDRX in S1-3 [47]. The development of LAGBs with a gradual increase in misorientation is the main feature of CDRX [77]. The fraction of HAGBs increased significantly from 0.3 in S4 to 0.55–0.62 in S1, S2 and S3 (Table 4), suggesting that generally DRX progressed much further in S1-S3 rather than in S4. A fraction of 0.7 LAGBs in S4 is related to the deactivation of CDRX in its third thermal cycle, as dynamically recovered grains cannot be transformed to DRX grains due to a high processing strain rate. As CDRX is accompanied by a consumption of LAGBs (Fig. 1), it can be confirmed that CDRX is not the main DRX mechanism in S4, as 70% of the grain boundaries remained as LAGBs. Both classical and thermostatistical approaches also showed that DDRX is activated during the third thermal cycle of S4. However, the ϵ_t is not high enough to promote large amounts of DDRX in the whole microstructure. This resulted in the evolution of a more inhomogeneous microstructure in S4, compared to S1-S3. Fig. 11b shows that only S1 and S4 are prone to DRV at their corresponding final thermal cycles. During this stage, the remaining deformed grains undergo DRV and at the same time the DRX grains formed at the previous stage can grow and increase their dislocation density. In addition to this, some of the cellular structures that have not the appropriate conditions for DRX/DRV may also coarsen and increase the deformed grains content in S1 and S4. Therefore, the microstructural evolution in each of the samples can be summarised as follows:

- S1: Highly deformed dendritic structure was formed during the first three thermal cycles in each layer. During the fourth cycle, CDRX occurred and HAGBs developed in the microstructure. In the fifth cycle, DRV activated and some of the deformed and recrystallized grains also undergo substructure development, resulting in a high fraction of substructured grains.
- S2 and S3: These samples respectively experience two and one rapid solidification/melting stages leading to the development of a highly deformed structure. They both undergo DRV followed by CDRX at their final thermal cycles. Higher recrystallized and HAGBs fractions in these samples compared with the other samples stem from the higher DRX progress and the absence of a thermal cycle undergoing DRV.
- S4: Highly deformed dendritic structure with a high dislocation density formed during the first and second thermal cycles. In the third thermal cycle, DRV activates as a precursor for CDRX, but due to high strain rate in this cycle, most of the grains undergo just DRV developing LAGBs. Incomplete DDRX was also activated, as the total strain was not sufficient for obtaining a fully recrystallized microstructure. This is the reason for a low fraction of HAGBs in this sample. Finally, the remaining highly deformed structure starts to grow at the fourth thermal cycle, as the conditions are not appropriate for DRX. They remain as deformed grains (red in Fig. 4d). Some of the recrystallized grains undergo DRV and become substructured grains (yellow in Fig. 4d). The dislocation density increases in these grains. The remaining DRV grains in the previous cycle undergo more DRV and grain growth, increasing the fraction of substructured grains. At the end, only 5% of the grains can be characterised as DRX grains with low dislocation density.

Results of the present study show that LAGBs played a significant role in the strengthening of LPBF processed 316L SS. The yield strength can, for the first time, be quantitatively related to the fraction of LAGBs. In order to prove this concept, three more samples produced by the AM125 machine (laser spot size of 70 μm) with other scan speeds (0.33 m/s, 0.56 m/s and 0.4 m/s) are accounted for to cover a wider range of LAGB fractions. The results related to S3 are not taken into account, due to its high porosity content. In addition to this, the results of previous studies on LPBF of 316L SS were also used for comparison and model verification [78–82]. The relationship between the LAGBs fraction (X_{LAGB}) and the yield strength of 316L SS processed with AM is shown in Fig. 13a. Therefore, the yield strength of LPBF-processed austenitic

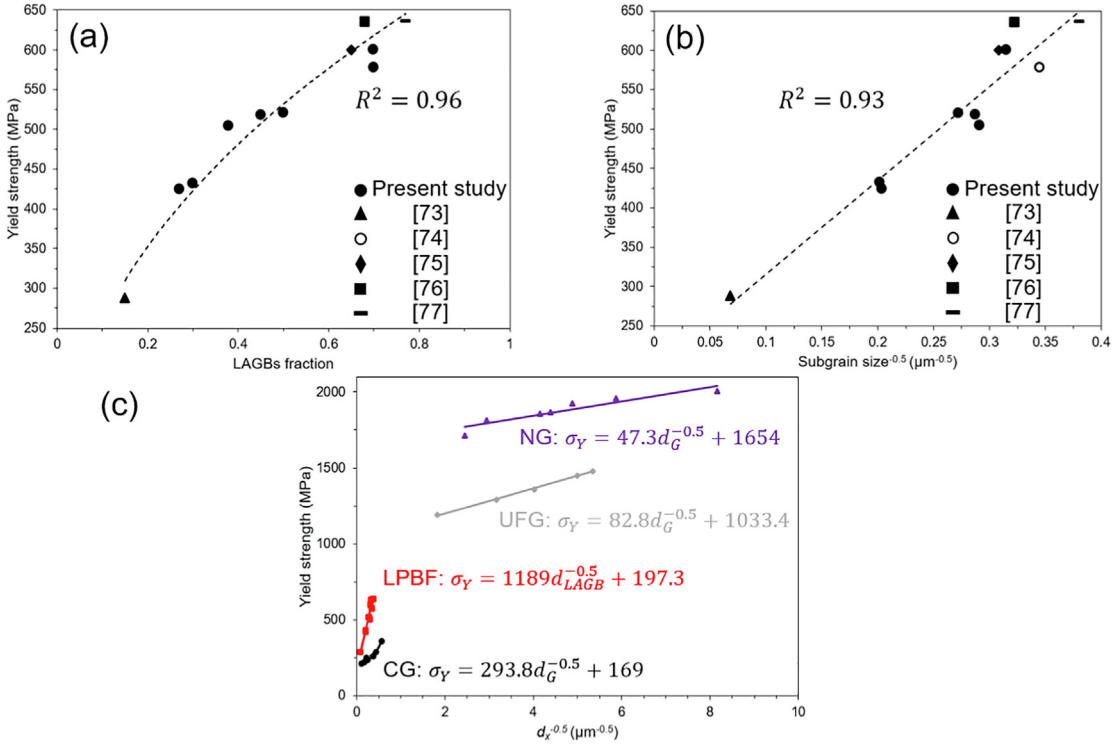

Fig. 13. (a) Effect of low-angle grain boundaries on the yield strength of 316L SS processed by AM. (b) Yield strength as a function of the inverse square root of subgrain size of LPBF 316L SS reported in the present work and in the literature. (c) Comparison of the Hall–Petch relationships reported for wrought 316L SS with various microstructures (CG: coarse grained, UFG: ultrafine grained and NG: nanograined) [83].

stainless steels that do not undergo phase transformation during processing depends on the LAGBs fraction:

$$\sigma_Y = 725.4X_{LAGB}^{0.45}. \quad (14)$$

Eq. (14) expresses the yield strength of AM produced 316L SS with an estimated error of 4%. The error may arise from the effect of porosity and residual stresses generated during LPBF. Eq. (14) highlights the significant role of substructures in strengthening of LPBF alloys, while in wrought products both the actual grains and substructures contribute to strengthening [32]. In contrast with the common approach for modelling strengthening mechanisms, which include separate terms for grain boundary, dislocations and substructure strengthening, a unified Hall–Petch-type relationship is suggested in this work, which makes it possible to relate processing-microstructure-properties through grain boundary engineering. It has been assumed that the subgrain size (d_{LAGB}, the size of the grains with low-angle boundaries) is equal to the product of the actual grain size (d_G, considering only HAGBs) and their relevant fraction (X_{HAGB}):

$$d_{LAGB} = d_G \cdot X_{HAGB} = d_G \cdot [1 - X_{LAGB}]. \quad (15)$$

This is due to the number of LAGB grains that can be accommodated in a HAGB grain is $(X_{HAGB})^{-1}$. Thus, $(X_{HAGB})^{-1} \cdot d_{LAGB} = d_G$. And grain boundary conservation demands $X_{LAGB} + X_{HAGB} = 1$, from which Eq. (15) emerges. As it is shown that the yield strength of LPBF processed 316L SS depends significantly on X_{LAGB}, it can be concluded that the yield strength can be interpretted as a Hall–Petch-type relationship considering only d_{LAGB}. The expression for LPBF 316L SS is fitted in Fig. 13b. Table 10 lists the data of the σ_Y, d_G, X_{LAGB} and X_{HAGB} for the modelled conditions.

Fig. 13b shows that the Hall–Petch equation for LPBF 316L SS based on the subgrain size relationship developed in this study (Eq. 15) agrees quite well with the theoretical linear relationship,

Table 10
Yield strength (σ_Y), high-angle boundary mean grain size (d_G), LAGBs fraction (X_{LAGB}) and HAGBs fraction (X_{HAGB}) for LPBF 316L SS from this study and literature.

σ_Y (MPa)	d_G (μm)	X_{LAGB}	X_{HAGB}	Reference
600	35	0.7	0.3	Present work
518	22	0.45	0.55	Present work
432	35	0.3	0.7	Present work
504	19	0.38	0.62	Present work
424	33	0.27	0.73	Present work
520	27	0.5	0.5	Present work
635	30	0.68	0.32	[78]
600	29	0.65	0.35	[79]
288	254	0.15	0.85	[80]
637	30	0.77	0.23	[81]
578	28	0.7	0.3	[82]

with an R^2=0.93. The Hall–Petch-type equation for LPBF 316L SS is determined as:

$$\sigma_Y = 197.3 + 1189d_{LAGB}^{-0.5}. \quad (16)$$

The Hall–Petch equations for nanostructured (NG region), ultrafine grained (UFG region) and coarse grained (CG region) wrought 316L SS, based on previous research by Yin et al. [83] are also shown in Fig. 13c. The values of the Hall–Petch constant and the friction stress for wrought and LPBF components are listed in Table 11. It can be seen that the Hall–Petch constant incresed significantly for LPBF 316L SS. Interestingly, the friction stress for LPBF and coarse-grained wrought 316L are similar (the slight difference can be attributed to higher N content in LPBF alloys compared to wrought components). However, the friction stress increased significantly by a decrease in the actual mean grain size. This means that grain refinement in wrought products lead to a significant increase in the dislocation density within the grains with

Table 11
Parameters of Hall–Petch-type equations for LPBF and wrought 316L SS components.

Processing	Hall–Petch constant (MPa μm$^{0.5}$)	Friction stress (MPa)
LPBF	1189	197.3
Wrought (CG)	293.8	169
Wrought (UFG)	82.8	1033.4
Wrought (NG)	47.3	1654

high-angle boundaries. In LPBF alloys, subgrains with low-angle boundaries contain a large dislocation density around LAGBs, which is in agreement with the microstructural characterisation performed by Hong *et al.* [79]. Therefore, LPBF results in significant LAGB strengthening. The Hall–Petch constant for LPBF alloys is 4, 15 and 29 times larger than coarse grained, ultrafine grained and nanograined 316L SS, respectively. This shows that subgrains in LPBF alloys are much stronger barriers to dislocation movement, compared with actual grain boundaries in the wrought alloys. Therefore, it can be concluded that in contrast with wrought alloys, where grain size has the most important influence on the yield strength, subgrain size (not the dislocation cell size) plays a vital role in strengthening of LPBF austenitic stainless steels, which have a columnar dendritic solidification structure.

The strengthening contribution of LAGBs is discussed already in the literature [31,10]. However, the present paper is the first publication which quantitatively shows the importance of LAGBs in strengthening of LPBF alloys. In the literature, the Hall–Petch relationship typically applies to HAGBs, but the results of this work show that there is no such relationship in LPBF alloys. Instead, there is a Hall–Petch-type relationship between subgrain size and the yield strength, which suggests that the strengthening efficiency of LAGBs in LPBF alloys is comparable to HAGBs in wrought alloys. Table 11 shows that subgrain boundaries (LAGBs) are very strong barriers to dislocation motion, as the Hall–Petch constant for LPBF alloy is 29 times larger than the nanostructured wrought material, which microstructure is dominated by HAGBs. This may be due to the strengthening effects that dislocation cells add to the LAGBs during DRV process, by rearrangement of highly dense dislocations into LAGBs, and mobile dislocations sliding along planes of orientation such that the LAGBs act as strong obstacles.

Previous reports in the literature claimed that solidification cellular structures are the main contributor to yield strengthening of LPBF FCC alloys [10,8]. Wang et al. [10] claimed that yield strength of LPBF alloys such as 316L SS is inversely proportional to the size of the solidification cellular structure (d_c) through the Hall–Petch relationship presented in Eq. (1). However, the results of this study show that there is no quantitative relationship between d_c and the yield strength of LPBF 316L SS. Comparing Tables 5 and 6 suggests that d_c in this study does not dictate yield strength, as S4 with the highest yield strength exhibits coarser d_c compared with S1, even S3, with the lowest yield strength. Moreover, using Eq. (1), the estimated yield strength for the samples produced in this work are 628, 517, 620, and 585 MPa, for S1, S2, S3, and S4, respectively, which are far from the experimental results (Table 6). Comparing our results with those reported by Wang *et al.* [10] is inappropriate, because despite the similar yield strength of S4 in our work (600 MPa) and the Concept machine sample in their work (590 MPa), the average d_c we observed is much finer than their sample (0.4 μm for S4 and 0.58 μm for Concept sample), which suggests that there is no solidification cell based Hall–Petch relationship between d_c and yield strength in LPBF alloys. The great differences of the estimated values for yield strength through Eq. (1) with experimental results also cannot be related to the porosity values, because a reduction of 220 MPa in the yield strength (in the case of S3) only because of lack-of-fusion pores is not reasonable, and such decrease in the yield strength due to porosity has not been reported previously. Moreover, the samples in [10] also contained porosity up to 0.8%, confirming that porosity has no significant influence on the yield strength of LPBF alloys when under 2%.

Similar to the theory of martensite strengthening [84–86], we showed that it is not always the finest microstructural feature that dictates the yield strength in LPBF alloys. Martensite has a hierarchical structure composed of packets, blocks, and laths with the size range decreasing from packets to laths [86]. LPBF alloys also have a hierarchy in their microstructures: actual grains, subgrains, and dislocation/solidification cells. Many researches showed that in martensite, block size, which is the middle-sized feature, dictates yield strength [84–86]. Galindo-Nava and Rivera-Díaz-del-Castillo [86] suggested that packets, blocks and laths are all interconnected and synergistically play important roles in microstructural evolution to determine the dislocation density of martensite. However, hardening appears to be dominated by the block size as the main source of strengthening through a Hall–Petch-type relationship. Previous reports also showed that there may be a Hall–Petch-type relationship between the packet size and yield strength, but the correlation is less precise compared to when block size is considered as the main effective barrier to dislocation motion. The results of this work show that there is a precise correlation between the subgrain size, as a middle-sized feature in hierarchy of LPBF microstructures, and the yield strength through a Hall–Petch-type relationship. Previously, Li et al. [11] tried to correlate the dislocation/solidification cell size to the resolved shear strength of 316L SS, using micropillar compression testing. However, the deviation of resolved shear yield stress was large (R^2=42%), which may reduce the reliability of those results. At the end, it is worth mentioning that dislocation cellular structures play a role in strengthening of LPBFed 316L SS by assisting on the formation of subgrains and LAGBs. High dislocation densities around cell walls also contribute to strengthening, which is considered to feature in the very high Hall–Petch-type constant that is obtained from this work (1189 MPa μm$^{0.5}$). Therefore, dislocation density and cell size play a role in strengthening of LPBFed 316L SS, but the most significant feature that dictates the yield strength is found to be the subgrains boundaries.

The evolution of LAGBs depends strongly on the development of DRV [87]. To control the occurrence of DRV during LPBF, two factors must be controlled: (i) process strain rate, and (ii) temperature gradients. According to the thermostatistical theory of plasticity [57], the transition between CDRX and DRV can be determined by controlling the process strain rate, as described by Eq. (8). The present results showed that the highest LAGB fraction is obtained when the set of process parameters yields a strain rate almost equal to $\dot{\epsilon}_c^T$. Thus, to maximise the yield strength, the following condition should be met:

$$\dot{\epsilon} = \frac{kT_{peak}\,v}{P} = (\dot{\epsilon}_0 + \vartheta)\exp\left(-\frac{\frac{\lambda}{2}\mu b^3 - \frac{2xl^*}{bk_c}\Delta G_{sys}}{k_B T}\right). \quad (17)$$

To increase the LAGB fraction, at least one thermal cycle, in which DRV can be activated directly is also needed. Hence, temperature gradients and subsequently δ and Δ must be controlled. The present results showed that to get a DRV-based thermal cycle, it is necessary to minimise δ and maximise Δ (Fig. 11b). Although too large Δ may cause lack of fusion. δ and Δ depend strongly on the layer thickness and the hatch distance, respectively (Eqs. (10) and (11)). Therefore, lower layer thickness and higher hatch distances can increase the strengthening potential of LPBF processed austenitic stainless steels.

5. Conclusions

Austenitic stainless steel laser powder bed fusion microstructures were correlated to their yield strength. The main conclusions can be summarised as follows:

1. Three restoration processes, discontinuous dynamic recrystallization, continuous dynamic recrystallization and dynamic recovery are found to be activated and control the final microstructure of as-built specimens produced with different process parameters.
2. Temperature–time profiles showed that the activation of restoration processes strongly depends on process parameters. The classical Zener-Hollomon and a thermostatistical approach were used to model the detailed restoration mechanisms. The sample, in which discontinuous dynamic recrystallization and dynamic recovery are activated, showed the highest yield strength upon tensile testing.
3. Dislocation cell structures form during the rapid solidification/melting cycles, contributing to the formation of low-angle grain boundaries and subgrains. Their presence is important, as they can determine the fraction of low-angle grain boundaries and subgrain size.
4. The yield strength of the laser powder bed fusion as-built samples does not follow the classical Hall–Petch relationship, which assumes that grain boundaries are the strongest dislocation movement barriers, as samples with very similar grain sizes show different yield strengths. Grain sizes in laser powder bed fusion should be considered in two categories: (i) the actual grains (those with high-angle boundaries) and (ii) the subgrains (grains with low-angle boundaries).
5. The yield strength could be expressed by the fraction of low-angle grain boundaries via a power law relationship. This led to the derivation of a unified Hall–Petch-type relationship, which relates the yield strength to the subgrain size, instead of the actual high-angle grain size. The relationship allows to control the yield strength of laser powder bed fusion 316L austenitic stainless steels through grain boundary engineering. Subgrain size refinement, which is achievable via increasing the fraction of low-angle grain boundaries, is suggested as the main approach for yield strength improvement in laser powder bed fusion of austenitic stainless steels. The presence of pores and residual stresses could result in deviations from the yield strength estimation.
6. Dislocation cell size and dislocation density contribute to yield strengthening of laser powder bed fusion 316L stainless steel; this results from increasing the strength of low-angle grain boundaries and subgrains. The effect is captured in the very high Hall–Petch-type constant of the laser powder bed fusion 316L stainless steel compared to wrought counterparts.
7. To maximise the yield strength of laser powder bed fusion processed austenitic stainless steels, the occurrence of dynamic recovery processes should be maximised to enhance the low-angle grain boundary fraction. This could be achieved by controlling the process strain rate (a criterion is suggested), and by controlling temperature gradients via decreasing the layer thickness and increasing the hatch distance.

Declaration of Competing Interest

The authors declare that they have no known competing financial interests or personal relationships that could have appeared to influence the work reported in this paper.

Acknowledgments

This work was supported by the Royal Academy of Engineering for chair funding (RCSRF1718/5/32), and by EPSRC via DARE grant (EP/L025213/1). HF acknowledges the support by National Natural Science Foundation of China (51971011) and Beihang Top Young Talent Support Programme (KG12079901).

Appendix A. Supplementary material

Supplementary data associated with this article can be found, in the online version, at https://doi.org/10.1016/j.matdes.2021.110246.

References

[1] J.A. Gonzalez, J. Mireles, S. Stafford, M.A. Perez, C.A. Terrazas, R.B. Wicker, Characterization of Inconel 625 fabricated using powder-bed-based additive manufacturing technologies, J. Mater. Process. Technol. 264 (2019) 200–210.
[2] J.P. Oliveira, A. LaLonde, J. Ma, Processing parameters in laser powder bed fusion metal additive manufacturing, Mater. Des. 193 (2020) 108762.
[3] J. Oliveira, T. Santos, R. Miranda, Revisiting fundamental welding concepts to improve additive manufacturing: from theory to practice, Prog. Mater. Sci. 107 (2020) 100590.
[4] H. Eskandari Sabzi, S. Maeng, X. Liang, M. Simonelli, N.T. Aboulkhair, P.E.J. Rivera-Díaz-del Castillo, Controlling crack formation and porosity in laser powder bed fusion: alloy design and process optimisation, Addit. Manuf. (2020) 101360.
[5] M.J. Heiden, L.A. Deibler, J.M. Rodelas, J.R. Koepke, D.J. Tung, D.J. Saiz, B.H. Jared, Addit. Manuf. 25 (2019) 84–103.
[6] W.E. King, H.D. Barth, V.M. Castillo, G.F. Gallegos, J.W. Gibbs, D.E. Hahn, C. Kamath, A.M. Rubenchik, Observation of keyhole-mode laser melting in laser powder-bed fusion additive manufacturing, J. Mater. Process. Technol. 214 (12) (2014) 2915–2925.
[7] H. Eskandari Sabzi, P.E.J. Rivera-Díaz-del Castillo, Composition and process parameter dependence of yield strength in laser powder bed fusion alloys, Mater. Des. (2020) 109024.
[8] D. Kong, C. Dong, S. Wei, X. Ni, L. Zhang, R. Li, L. Wang, C. Man, X. Li, About metastable cellular structure in additively manufactured austenitic stainless steels, Addit. Manuf. (2020) 101804.
[9] K. Bertsch, G.M. de Bellefon, B. Kuehl, D. Thoma, Origin of dislocation structures in an additively manufactured austenitic stainless steel 316L, Acta Mater. 199 (2020) 19–33.
[10] Y.M. Wang, T. Voisin, J.T. McKeown, J. Ye, N.P. Calta, Z. Li, Z. Zeng, Y. Zhang, W. Chen, T.T. Roehling, et al., Additively manufactured hierarchical stainless steels with high strength and ductility, Nat. Mater. 17 (1) (2018) 63–71.
[11] Z. Li, B. He, Q. Guo, Strengthening and hardening mechanisms of additively manufactured stainless steels: The role of cell sizes, Scr. Mater. 177 (2020) 17–21.
[12] K. Saeidi, X. Gao, Y. Zhong, Z.J. Shen, Hardened austenite steel with columnar sub-grain structure formed by laser melting, Mater. Sci. Eng. A. 625 (2015) 221–229.
[13] D. Ramirez, L. Murr, E. Martinez, D. Hernandez, J. Martinez, B.I. Machado, F. Medina, P. Frigola, R. Wicker, Novel precipitate–microstructural architecture developed in the fabrication of solid copper components by additive manufacturing using electron beam melting, Acta Mater. 59 (10) (2011) 4088–4099.
[14] Y.S.J. Yoo, T.A. Book, M.D. Sangid, J. Kacher, Identifying strain localization and dislocation processes in fatigued inconel 718 manufactured from selective laser melting, Mater. Sci. Eng. A. 724 (2018) 444–451.
[15] K.E. Huang, R.E. Logé, A review of dynamic recrystallization phenomena in metallic materials, Mater. Des. 111 (2016) 548–574.
[16] T. DebRoy, H.L. Wei, J.S. Zuback, T. Mukherjee, J.W. Elmer, J.O. Milewski, A.M. Beese, A.d. Wilson-Heid, A. De, W. Zhang, Additive manufacturing of metallic components–process, structure and properties, Prog. Mater. Sci. 92 (2018) 112–224.
[17] T. Sakai, A. Belyakov, R. Kaibyshev, H. Miura, J.J. Jonas, Dynamic and post-dynamic recrystallization under hot, cold and severe plastic deformation conditions, Prog. Mater. Sci. 60 (2014) 130–207.
[18] Z. Yanushkevich, A. Belyakov, R. Kaibyshev, Microstructural evolution of a 304-type austenitic stainless steel during rolling at temperatures of 773–1273 K, Acta. Mater. 82 (2015) 244–254.
[19] M. Tikhonova, R. Kaibyshev, A. Belyakov, Microstructure and mechanical properties of austenitic stainless steels after dynamic and post-dynamic recrystallization treatment, Adv. Eng. Mater. 20 (7) (2018) 1700960.
[20] H.R. Abedi, A.Z. Hanzaki, Z. Liu, R. Xin, N. Haghdadi, P.D. Hodgson, Continuous dynamic recrystallization in low density steel, Mater. Des. 114 (2017) 55–64.

[21] M. El Wahabi, L. Gavard, F. Montheillet, J.M. Cabrera, J.M. Prado, Effect of initial grain size on dynamic recrystallization in high purity austenitic stainless steels, Acta. Mater. 53 (17) (2005) 4605–4612.
[22] S.V. Dobatkin, Severe plastic deformation of steels: structure, properties and techniques, in: Investigations and Applications of Severe Plastic Deformation, Springer, 2000, pp. 13–22.
[23] T. Sakai, A. Belyakov, H. Miura, Ultrafine grain formation in ferritic stainless steel during severe plastic deformation, Metall. Mater. Trans. A. 39 (9) (2008) 2206.
[24] N. Hansen, Hall-Petch relation and boundary strengthening, Scr. Mater. 51 (8) (2004) 801–806.
[25] U.F. Kocks, H. Mecking, Physics and phenomenology of strain hardening: the FCC case, Prog. Mater. Sci. 48 (3) (2003) 171–273.
[26] A. Hadadzadeh, C. Baxter, B.S. Amirkhiz, M. Mohammadi, Strengthening mechanisms in direct metal laser sintered AlSi10Mg: Comparison between virgin and recycled powders, Addit. Manuf. 23 (2018) 108–120.
[27] R. Li, M. Wang, Z. Li, P. Cao, T. Yuan, H. Zhu, Developing a high-strength Al-Mg-Si-Sc-Zr alloy for selective laser melting: crack-inhibiting and multiple strengthening mechanisms, Acta. Mater. (2020).
[28] A. Hadadzadeh, A. Shahriari, B.S. Amirkhiz, J. Li, M. Mohammadi, Additive manufacturing of an Fe–Cr–Ni–Al maraging stainless steel: Microstructure evolution, heat treatment, and strengthening mechanisms, Mater. Sci. Eng. A. 139470 (2020).
[29] Z.G. Zhu, Q.B. Nguyen, F.L. Ng, X.H. An, X.Z. Liao, P.K. Liaw, S.M.L. Nai, J. Wei, Hierarchical microstructure and strengthening mechanisms of a CoCrFeNiMn high entropy alloy additively manufactured by selective laser melting, Scr. Mater. 154 (2018) 20–24.
[30] Q. Jia, P. Rometsch, P. Kürnsteiner, Q. Chao, A. Huang, M. Weyland, L. Bourgeois, X. Wu, Selective laser melting of a high strength AlMnSc alloy: Alloy design and strengthening mechanisms, Acta. Mater. 171 (2019) 108–118.
[31] T. Voisin, J.-B. Forien, A. Perron, S. Aubry, N. Bertin, A. Samanta, A. Baker, Y.M. Wang, New insights on cellular structures strengthening mechanisms and thermal stability of an austenitic stainless steel fabricated by laser powder-bed-fusion, Acta Mater. 203 (2021) 116476.
[32] Z. Yanushkevich, S.V. Dobatkin, A. Belyakov, R. Kaibyshev, Hall-Petch relationship for austenitic stainless steels processed by large strain warm rolling, Acta. Mater. 136 (2017) 39–48.
[33] T. Kurzynowski, K. Gruber, W. Stopyra, B. Kuźnicka, E. Chlebus, Correlation between process parameters, microstructure and properties of 316L stainless steel processed by selective laser melting, Mater. Sci. Eng. A. 718 (2018) 64–73.
[34] H. Eskandari Sabzi, N.T. Aboulkhair, X. Liang, X.-H. Li, M. Simonelli, H. Fu, P.E.J. Rivera-Díaz-del Castillo, Grain refinement in laser powder bed fusion: The influence of dynamic recrystallization and recovery, Mater. Des. (2020) 109181.
[35] D. Hann, J. Iammi, J. Folkes, A simple methodology for predicting laser-weld properties from material and laser parameters, J. Phys. D. Appl. Phys. 44 (44) (2011) 445401.
[36] J.-O. Andersson, T. Helander, L. Höglund, P. Shi, B. Sundman, Thermo-calc & DICTRA, computational tools for materials science, CALPHAD 26 (2) (2002) 273–312.
[37] C.A. Schneider, W.S. Rasband, K.W. Eliceiri, NIH image to ImageJ: 25 years of image analysis, Nat. Methods. 9 (7) (2012) 671.
[38] H. Farnoush, A. Momeni, K. Dehghani, J.A. Mohandesi, H. Keshmiri, Hot deformation characteristics of 2205 duplex stainless steel based on the behavior of constituent phases, Mater. Des. 31 (1) (2010) 220–226.
[39] N. Ryan, H. McQueen, Flow stress, dynamic restoration, strain hardening and ductility in hot working of 316 steel, J. Mater. Process. Technol. 21 (2) (1990) 177–199.
[40] U. Andrade, M. Meyers, K. Vecchio, A.H. Chokshi, Dynamic recrystallization in high-strain, high-strain-rate plastic deformation of copper, Acta Metall. 42 (9) (1994) 3183–3195.
[41] A. Hadadzadeh, B.S. Amirkhiz, J. Li, A. Odeshi, M. Mohammadi, Deformation mechanism during dynamic loading of an additively manufactured alsi10mg_200c, Mater. Sci. Eng. A. 722 (2018) 263–268.
[42] M.-H. Wang, Y.-F. Li, W.-H. Wang, J. Zhou, A. Chiba, Quantitative analysis of work hardening and dynamic softening behavior of low carbon alloy steel based on the flow stress, Mater. Des. 45 (2013) 384–392.
[43] H. McQueen, C. Imbert, Dynamic recrystallization: plasticity enhancing structural development, J. Alloys. Comp. 378 (1–2) (2004) 35–43.
[44] M. Azarbarmas, S.S. Mirjavadi, A. Ghasemi, A.M. Hamouda, A combined method to model dynamic recrystallization based on cellular automaton and a phenomenological (cap) approach, Metals 8 (11) (2018) 923.
[45] H. McQueen, S. Yue, N. Ryan, E. Fry, Hot working characteristics of steels in austenitic state, J. Mater. Process. Technol. 53 (1–2) (1995) 293–310.
[46] F.J. Humphreys, M. Hatherly, Recrystallization and related annealing phenomena, Elsevier, 2012.
[47] S. Gourdet, F. Montheillet, A model of continuous dynamic recrystallization, Acta. Mater. 51 (9) (2003) 2685–2699.
[48] P. Bernard, S. Bag, K. Huang, R.E. Logé, A two-site mean field model of discontinuous dynamic recrystallization, Mater. Sci. Eng. A 528 (24) (2011) 7357–7367.
[49] K.A. Babu, Y.H. Mozumder, R. Saha, V.S. Sarma, S. Mandal, Hot-workability of super-304h exhibiting continuous to discontinuous dynamic recrystallization transition, Mater. Sci. Eng. A. 734 (2018) 269–280.
[50] X.-G. Liu, L.-G. Zhang, R.-S. Qi, L. Chen, M. Jin, B.-F. Guo, Prediction of critical conditions for dynamic recrystallization in 316LN austenitic steel, J. Iron. Steel Res. Int. 23 (3) (2016) 238–243.
[51] R. Puli, G.J. Ram, Dynamic recrystallization in friction surfaced austenitic stainless steel coatings, Mater. Charact. 74 (2012) 49–54.
[52] W. Jiang, Y. Zhang, W. Woo, Using heat sink technology to decrease residual stress in 316L stainless steel welding joint: Finite element simulation, Int. J. Pressure. Vessels. Piping. 92 (2012) 56–62.
[53] E. Galindo-Nava, P.E.J. Rivera-Díaz-del Castillo, Grain size evolution during discontinuous dynamic recrystallization, Scr. Mater. 72 (2014) 1–4.
[54] E. Puchi Cabrera, High temperature deformation of 316L stainless steel, Mater. Sci. Technol. 17 (2) (2001) 155–161.
[55] C. Robertson, M. Fivel, A. Fissolo, Dislocation substructure in 316L stainless steel under thermal fatigue up to 650 K, Mater. Sci. Eng. A. 315 (1–2) (2001) 47–57.
[56] L.M. Headings, K. Kotian, M.J. Dapino, Speed of sound measurement in solids using polyvinylidene fluoride (PVDF) sensors, Smart Materials, Adaptive Structures and Intelligent Systems, vol. 56031, American Society of Mechanical Engineers, 2013. p. V001T04A012.
[57] E. Galindo-Nava, P.E.J. Rivera-Díaz-del Castillo, Thermostatistical modelling of hot deformation in fcc metals, Int. J. Plast. 47 (2013) 202–221.
[58] M.-S. Pham, B. Dovgyy, P.A. Hooper, C.M. Gourlay, A. Piglione, The role of side-branching in microstructure development in laser powder-bed fusion, Nat. Commun. 11 (1) (2020) 1–12.
[59] H. Hu, L. Zhen, L. Yang, W. Shao, B. Zhang, Deformation behavior and microstructure evolution of 7050 aluminum alloy during high temperature deformation, Mater. Sci. Eng. A. 488 (1–2) (2008) 64–71.
[60] S. Sui, C. Zhong, J. Chen, A. Gasser, W. Huang, J.H. Schleifenbaum, Influence of solution heat treatment on microstructure and tensile properties of Inconel 718 formed by high-deposition-rate laser metal deposition, J. Alloys Comp. 740 (2018) 389–399.
[61] L. Tan, Y. Li, F. Liu, Y. Nie, L. Jiang, Microstructure evolutions of a powder metallurgy superalloy during high-strain-rate deformation, J. Alloys Comp. 789 (2019) 506–517.
[62] B.-R. Chen, A.-C. Yeh, J.-W. Yeh, Effect of one-step recrystallization on the grain boundary evolution of cocrfemnni high entropy alloy and its subsystems, Sci. Rep. 6 (1) (2016) 1–9.
[63] T. Konkova, S. Rahimi, S. Mironov, T. Baker, Effect of strain level on the evolution of microstructure in a recently developed AD730 nickel based superalloy during hot forging, Mater. Charact. 139 (2018) 437–445.
[64] S. Gourdet, F. Montheillet, An experimental study of the recrystallization mechanism during hot deformation of aluminium, Mater. Sci. Eng. A. 283 (1–2) (2000) 274–288.
[65] D. Lin, L. Xu, H. Jing, Y. Han, L. Zhao, F. Minami, Effects of annealing on the structure and mechanical properties of FeCoCrNi high-entropy alloy fabricated via selective laser melting, Addit. Manuf. 32 (2020) 101058.
[66] H. Hyer, L. Zhou, A. Mehta, S. Park, T. Huynh, S. Song, Y. Bai, K. Cho, B. McWilliams, Y. Sohn, Composition-dependent solidification cracking of aluminum-silicon alloys during laser powder bed fusion, Acta Mater. 208 (2021) 116698.
[67] U.S. Bertoli, B.E. MacDonald, J.M. Schoenung, Stability of cellular microstructure in laser powder bed fusion of 316l stainless steel, Mater. Sci. Eng. A. 739 (2019) 109–117.
[68] C. Zhao, K. Fezzaa, R.W. Cunningham, H. Wen, F. Carlo, L. Chen, A.D. Rollett, T. Sun, Real-time monitoring of laser powder bed fusion process using high-speed x-ray imaging and diffraction, Sci. Rep. 7 (1) (2017) 3602.
[69] B. Barkia, P. Aubry, P. Haghi-Ashtiani, T. Auger, L. Gosmain, F. Schuster, H. Maskrot, On the origin of the high tensile strength and ductility of additively manufactured 316L stainless steel: Multiscale investigation, J. Mater. Sci. Technol. 41 (2020) 209–218.
[70] T. Ronneberg, C.M. Davies, P.A. Hooper, Revealing relationships between porosity, microstructure and mechanical properties of laser powder bed fusion 316L stainless steel through heat treatment, Mater. Des. 189 (2020) 108481.
[71] E.W. Jost, J.C. Miers, A. Robbins, D.G. Moore, C. Saldana, Effects of spatial energy distribution-induced porosity on mechanical properties of laser powder bed fusion 316L stainless steel, Addit. Manuf. 39 (2021) 101875.
[72] R. Seede, D. Shoukr, B. Zhang, A. Whitt, S. Gibbons, P. Flater, A. Elwany, R. Arroyave, I. Karaman, An ultra-high strength martensitic steel fabricated using selective laser melting additive manufacturing: Densification, microstructure, and mechanical properties, Acta. Mater. 186 (2020) 199–214.
[73] Y. Chew, G. Bi, Z. Zhu, F. Ng, F. Weng, S. Liu, S. Nai, B. Lee, Microstructure and enhanced strength of laser aided additive manufactured CoCrFeNiMn high entropy alloy, Mater. Sci. Eng. A. 744 (2019) 137–144.
[74] P. Liu, X. Cui, J. Deng, S. Li, Z. Li, L. Chen, Investigation of thermal responses during metallic additive manufacturing using a "tri-prism" finite element method, Int. J. Thermal. Sci. 136 (2019) 217–229.
[75] A. Elmesalamy, J. Francis, L. Li, A comparison of residual stresses in multi pass narrow gap laser welds and gas-tungsten arc welds in AISI 316L stainless steel, Int. J. Pressure. Vessels. Piping. 113 (2014) 49–59.
[76] J. Oliveira, A. Cavaleiro, N. Schell, A. Stark, R. Miranda, J. Ocana, F.B. Fernandes, Effects of laser processing on the transformation characteristics of niti: A contribute to additive manufacturing, Scr. Mater. 152 (2018) 122–126.
[77] J.C. Tan, M.J. Tan, Dynamic continuous recrystallization characteristics in two stage deformation of Mg–3Al–1Zn alloy sheet, Mater. Sci. Eng. A. 339 (1–2) (2003) 124–132.

[78] Z. Li, T. Voisin, J.T. McKeown, J. Ye, T. Braun, C. Kamath, W.E. King, Y.M. Wang, Tensile properties, strain rate sensitivity, and activation volume of additively manufactured 316L stainless steels, Int. J. Plast. 120 (2019) 395–410.
[79] Y. Hong, C. Zhou, Y. Zheng, L. Zhang, J. Zheng, X. Chen, B. An, Formation of strain-induced martensite in selective laser melting austenitic stainless steel, Mater. Sci. Eng. A. 740 (2019) 420–426.
[80] F. Khodabakhshi, M. Farshidianfar, A. Gerlich, M. Nosko, V. Trembošová, A. Khajepour, Effects of laser additive manufacturing on microstructure and crystallographic texture of austenitic and martensitic stainless steels, Addit. Manuf. 31 (2020) 100915.
[81] D. Kong, C. Dong, X. Ni, L. Zhang, J. Yao, C. Man, X. Cheng, K. Xiao, X. Li, Mechanical properties and corrosion behavior of selective laser melted 316L stainless steel after different heat treatment processes, J. Mater. Sci. Technol. 35 (7) (2019) 1499–1507.
[82] Y. Hong, C. Zhou, Y. Zheng, L. Zhang, J. Zheng, The cellular boundary with high density of dislocations governed the strengthening mechanism in selective laser melted 316L stainless steel, Mater. Sci. Eng. A. (2020) 140279.
[83] F. Yin, G.J. Cheng, R. Xu, K. Zhao, Q. Li, J. Jian, S. Hu, S. Sun, L. An, Q. Han, Ultrastrong nanocrystalline stainless steel and its Hall-Petch relationship in the nanoscale, Scr. Mater. 155 (2018) 26–31.
[84] S. Morito, H. Yoshida, T. Maki, X. Huang, Effect of block size on the strength of lath martensite in low carbon steels, Mater. Sci. Eng. A. 438 (2006) 237–240.
[85] A. Shibata, T. Nagoshi, M. Sone, S. Morito, Y. Higo, Evaluation of the block boundary and sub-block boundary strengths of ferrous lath martensite using a micro-bending test, Mater. Sci. Eng. A. 527 (29–30) (2010) 7538–7544.
[86] E. Galindo-Nava, P. Rivera-Díaz-del Castillo, A model for the microstructure behaviour and strength evolution in lath martensite, Acta. Mater. 98 (2015) 81–93.
[87] C. Pithan, T. Hashimoto, M. Kawazoe, J. Nagahora, K. Higashi, Microstructure and texture evolution in ECAE processed A5056, Mater. Sci. Eng. A. 280 (1) (2000) 62–68.